

Geophysical methods reveal the soil architecture and subsurface stratigraphic heterogeneities across land-lake interfaces along Lake Erie

Solomon Ehosioko¹, Moses B Adebayo², Vanessa Bailey³, Roberta Bittencourt Peixoto², Efemena D Emmanuel², Fausto Machado-Silva², Peter Regier⁴, Trisha Spanbauer⁵, Shan Pushpajom Thomas², Nicholas Ward³, Michael Weintraub², and Kennedy Okioghene Doro²

¹University of Toledo

²University of Toledo

³Pacific Northwest National Laboratory (DOE)

⁴Marine and Coastal Research Laboratory, Pacific Northwest National Laboratory

⁵Unknown

October 17, 2023

Abstract

The land-lake interface is a unique zone where terrestrial and aquatic ecosystems meet, forming part of the Earth's most geochemically and biologically active zones. The unique characteristics of this interface are yet to be properly understood due to the inherently high spatiotemporal variability of subsurface properties, which are difficult to capture with the traditional soil sampling methods. Geophysical methods offer non-invasive techniques to capture variabilities in soil properties at a high resolution across various spatiotemporal scales. We combined electromagnetic induction (EMI), electrical resistivity tomography (ERT), and ground penetrating radar (GPR) with data from soil cores and in-situ sensors to investigate hydrostratigraphic heterogeneities across land-lake interfaces along the western basin of Lake Erie. Our Apparent electrical conductivity (ECa) maps matched soil maps from a public database with the hydric soil units delineated as high conductivity zones (ECa > 40 mS/m) and also detected additional soil units that were missed in the traditional soil maps. This implies that electromagnetic induction (EMI) could be relied upon for non-invasive characterization of soils in sampling-restricted sites where only non-invasive measurements are feasible. Results from ERT and GPR are consistent with the surficial geology of the study area and revealed variation in the vertical silty-clay and till sequence down to 3.5 m depth. These results indicate that multiple geophysical methods can be used to extrapolate soil properties and map stratigraphic structures at land-lake interfaces, thereby providing the missing information required to improve the earth system model (ESM) of coastal interfaces.

Hosted file

976524_0_art_file_11479725_s24z4q.docx available at <https://authorea.com/users/674120/articles/672611-geophysical-methods-reveal-the-soil-architecture-and-subsurface-stratigraphic-heterogeneities-across-land-lake-interfaces-along-lake-erie>

Hosted file

976524_0_supp_11479495_s24494.docx available at <https://authorea.com/users/674120/articles/672611-geophysical-methods-reveal-the-soil-architecture-and-subsurface-stratigraphic-heterogeneities-across-land-lake-interfaces-along-lake-erie>

1 **Geophysical methods reveal the soil architecture and subsurface stratigraphic**
2 **heterogeneities across land-lake interfaces along Lake Erie**

3 **Solomon Ehosioko^{1*}, Moses B. Adebayo¹, Vanessa L. Bailey^{2,1}, Roberta Bittencourt**
4 **Peixoto¹, Efemena D. Emmanuel¹, Fausto Machado-Silva¹, Peter J. Regier³, Trisha**
5 **Spanbauer¹, Shan Pushpajom Thomas¹, Nicholas D. Ward^{3,4}, Michael N. Weintraub^{1,2},**
6 **Kennedy O. Doro^{1*}**

7 ¹Department of Environmental Sciences, University of Toledo, OH, USA

8 ²Biological Sciences Division, Pacific Northwest National Laboratory, Richland, WA, USA

9 ³Coastal Sciences Division, Pacific Northwest National Laboratory, Sequim, WA, USA

10 ⁴College of the Environment, University of Washington, Seattle, WA, USA

11 ***Corresponding Author:** Solomon Ehosioko (solomon.ehosioko@utoledo.edu) and Kennedy O.
12 Doro (kennedy.doro@utoledo.edu)

13

14 **Key Points:**

- 15 • Multiple geophysical methods were combined to investigate hydrostratigraphic
16 heterogeneities across land-lake interfaces
- 17 • Apparent electrical conductivity maps matched soil maps from public database, with
18 hydric soil units delineated as high conductivity zones
- 19 • Results from resistivity and radar methods are consistent with the surficial geology of the
20 study area

21

22

23

24

25 **Abstract**

26 The land-lake interface is a unique zone where terrestrial and aquatic ecosystems meet, forming
27 part of the Earth's most geochemically and biologically active zones. The unique characteristics
28 of this interface are yet to be properly understood due to the inherently high spatiotemporal
29 variability of subsurface properties, which are difficult to capture with the traditional soil
30 sampling methods. Geophysical methods offer non-invasive techniques to capture variabilities in
31 soil properties at a high resolution across various spatiotemporal scales. We combined
32 electromagnetic induction (EMI), electrical resistivity tomography (ERT), and ground penetrating
33 radar (GPR) with data from soil cores and in-situ sensors to investigate hydrostratigraphic
34 heterogeneities across land-lake interfaces along the western basin of Lake Erie. Our Apparent
35 electrical conductivity (ECa) maps matched soil maps from a public database with the hydric soil
36 units delineated as high conductivity zones ($ECa > 40$ mS/m) and also detected additional soil
37 units that were missed in the traditional soil maps. This implies that electromagnetic induction
38 (EMI) could be relied upon for non-invasive characterization of soils in sampling-restricted sites
39 where only non-invasive measurements are feasible. Results from ERT and GPR are consistent
40 with the surficial geology of the study area and revealed variation in the vertical silty-clay and till
41 sequence down to 3.5 m depth. These results indicate that multiple geophysical methods can be
42 used to extrapolate soil properties and map stratigraphic structures at land-lake interfaces, thereby
43 providing the missing information required to improve the earth system model (ESM) of coastal
44 interfaces.

45

46

47

48

49 **Plain Language Summary**

50 The interface between land and lake is a very active zone where various geochemical and
51 biological changes occur. The unique characteristics of this interface are not fully understood
52 because subsurface properties vary in time and space, and thus difficult to measure with the
53 traditional soil sampling methods. We used three geophysical methods and data from soil cores
54 and in-situ sensors to investigate hydrological and stratigraphic heterogeneities across land-lake
55 interfaces along the western basin of Lake Erie. Our electrical conductivity maps matched soil
56 maps from a public database and also detected additional soil units that were missed in the
57 traditional soil maps, and the high conductivity zones matched the hydric soil units. Additionally,
58 our results from electrical resistivity and radar methods are consistent with the surficial geology
59 of the study area and revealed variation in the vertical silty-clay and till sequence down to 3.5 m
60 depth. This shows that electromagnetic induction could be used to characterize soils in sampling-
61 restricted sites where only non-invasive measurements are feasible. We also show that multiple
62 geophysical methods can be used to deduce soil properties and map stratigraphic structures at
63 land-lake interfaces, this information is required to improve the earth system model of coastal
64 interfaces.

65

66

67

68

69

70 **1. Introduction**

71 Soils are known to be very heterogeneous due to the variability in soil properties or soil
72 taxonomic classes within an area (Maestre and Cortina, 2002; McBratney and Minasny, 2007),
73 resulting from regional soil formation factors such as topography, parent material, climate,
74 organisms and time (ODNR, 2018; Sposito 2023). At land-lake interfaces, or more generally
75 terrestrial-aquatic interfaces (TAIs), heterogeneity in soil architecture is much more diverse. This
76 is because the TAI is where terrestrial and aquatic ecosystems meet and interact, forming an
77 active and dynamic zone where various hydrological and biogeochemical exchanges occur at
78 various spatial and temporal scales, thereby introducing additional sources of heterogeneity in the
79 TAI soils. The diverse heterogeneities embodied by coastal TAIs are usually not accounted for in
80 current earth system models (ESMs) (Ward et al. 2020).

81 Soil architecture which refers to the close relationship between the arrangement of soil physical
82 components in space and the functioning that such arrangement enables (Baveye et al. 2018;
83 Vogel et al. 2022), is controlled by the spatial configuration of pore networks resulting from
84 processes of root growth, wetting and drying dynamics, freeze-thawing cycles, tillage operations
85 (Dexter 1988, Vogel et al. 2022). Other factors that control soil architecture include the metabolic
86 activities of soil micro and macro fauna within a soil matrix, the cementing organic molecules
87 and associated physicochemical exchanges (Dexter 1988, Vogel et al. 2022). Soil architecture
88 thus serves as a complex heterogeneous biogeochemical interface that forms the basis for various
89 soil functions such as water retention, root growth, nutrient cycling, carbon storage, functional
90 biodiversity, solute transport, and contaminant degradation (Totsche et al. 2010; Vogel et al.
91 2022). The extent to which these factors will influence the soil architecture depends on the soil
92 type as well as the characteristics of the ecosystem unit or study site. Although these key

93 processes that control soil architecture occur mostly at the pore scale, their effects extend to
94 larger spatial scales (e.g., site to regional scales), as many hydrological and ecological soil
95 functions are governed by the soil architecture (Stewart et al. 1990; Romero-Ruiz et al. 2019).

96 Soil architecture has been investigated either by the aggregate approach or the pore approach.
97 The aggregate approach targets the stability and composition of isolated solid fragments, while
98 the pore approach targets the pore structure as well as the pore-solid interfaces in undisturbed
99 samples (Rabot et al. 2018; Vogel et al. 2022). The aggregate approach is challenged by the
100 limited understanding of how matter and energy fluxes through the soil will be affected when
101 isolated from the original soil matrix. It is expected that fluxes of liquid, gas, or nutrients will
102 differ between an isolated soil volume compared to an undisturbed one (e.g. Kravchenko et al.
103 2019). The pore approach considers the importance of spatial position but just within the context
104 of an undisturbed sample. Although the pore approach recognized that flow and mixing processes
105 such as diffusion of dissolved organic carbon, bioturbation, and pore water dynamics create
106 spatial heterogeneity in soil architecture, it does not account for such heterogeneity beyond
107 limited core samples (e.g. Young et al. 2001).

108 Traditional methods of soil investigation, such as soil cores, hand augers, excavation, or sensors
109 (e.g., Osborne and DeLaune, 2013) are point measurements that lack spatial resolution and may
110 not adequately capture the spatial variabilities necessary to include in site to global scale models.
111 Geophysical methods offer non-invasive techniques to capture spatial variability in soil properties
112 at high resolution and across various spatiotemporal scales (e.g., Besson et al. 2013; Krueger et
113 al. 2013; Emmanuel et al. 2023). Romero-Ruiz et al. (2018) reviewed the potential of harnessing
114 geophysical techniques for the characterization of soil architecture and identified geoelectrical
115 and electromagnetic methods among a spectrum of geophysical methods as ideal for soil

116 architecture characterization. Due to their sensitivity to soil hydrological states, these methods,
117 such as electromagnetic imaging (EMI) (e.g. Corwin and Lesch, 2005; Brechet et al. 2012;
118 Doolittle and Brevik, 2014; Emmanuel et al. 2023), electrical resistivity tomography (ERT) (e.g.
119 Michot et al. 2003; Kizhlo and Kanbergs, 2009; Besson et al. 2004, 2013; Doro et al. 2013),
120 induced polarization (IP) (e.g. Kemna et al. 2012; Kessouri et al. 2019), and ground penetrating
121 radar (GPR) (e.g. Grote et al. 2003; Krueger et al. 2013) have the capacity to assess the soil pore
122 space and how its varied distributions will affect soil hydrology.

123 Although geophysical methods have the potential to provide the high-resolution understanding of
124 soil spatiotemporal variabilities needed to improve representation of coastal TAIs in ESMS, this
125 approach is yet to be fully explored because most geophysical investigations of soil are focused
126 on purely terrestrial ecosystems. In this study, we combined three geophysical methods (EMI,
127 ERT, and GPR) with borehole information, as well as soil sensor and groundwater data, to
128 characterize soil architectural properties across land-lake interfaces along Lake Erie. This
129 approach provides a non-invasive and detailed characterization of TAI soils at high
130 spatiotemporal resolution, which is usually lacking with point sampling approaches. Combining
131 different geophysical methods is useful to understand both the lateral (using EMI) and vertical
132 (using ERT and GPR) variations in soil properties across the TAI. This approach could precisely
133 direct sampling and monitoring campaigns, replacing haphazard sampling and providing essential
134 data for constraining pedophysical and hydrological models across the TAIs. Here, we used a
135 variety of geophysical techniques to test the hypothesis that soil properties will show both
136 vertical and horizontal heterogeneity across land-lake interfaces.

137

138 **2. Study Area**

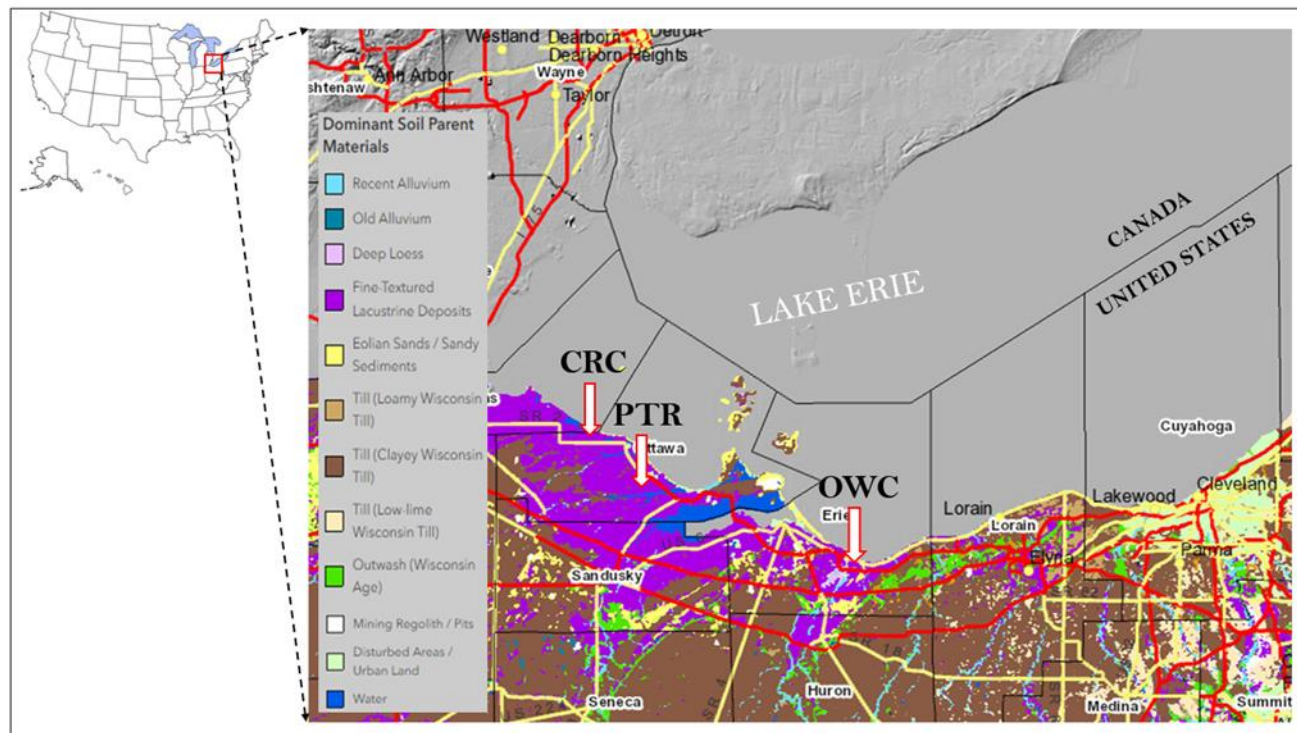
139
140 Our study sites are situated along the western-central basin of Lake Erie, the fourth largest of the
141 five Great Lakes in North America and the eleventh largest lake globally (Hansen, 1989). Lake
142 Erie is located on the international boundary between the United States and Canada. The northern
143 shore is bounded by the Ontario province of Canada, while the U.S. states of Michigan, Ohio,
144 Pennsylvania, and New York bounds the western, southern, and eastern shores. The three study
145 sites, Crane Creek (CRC), Portage River (PTR), and Old woman creek (OWC) (Figure 1), are
146 located in the North West Ohio portion of the Western Lake Erie Basin (WLEB) which is one of
147 United States' most significant collections of inland rivers and streams. The WLEB covers
148 nearly 7 million acres and stretches across most of northwest Ohio, portions of northeast Indiana,
149 and southeast Michigan. Around 75 percent of the land is used for agricultural
150 production. Approximately 1.2 million people live in the basin, distributed between three urban
151 centers, Toledo, Ohio; Fort Wayne, Indiana; Lima, Ohio, and numerous cities and towns.

152 The geology of the Lake Erie region is characterized by middle Paleozoic sedimentary rocks
153 composed of limestones, dolomites, shales, and sandstones (Bolsenga and Herdendorf 1993).
154 These rocks were deposited about 430 to 300 million years ago under conditions ranging from
155 tropical barrier reef habitats to deltaic and deepwater clastic environments associated with
156 mountain building (orogenic) episodes and tectonic plate collisions (Herdendorf, 2013). These
157 episodes and the resulting uplifts ushered in a long period of erosion which led to the excavation
158 of deep stream valleys and a mature drainage system along the longitudinal axis of the present
159 lake. Continental glaciers during late Cenozoic Era (Pleistocene Epoch beginning about 2.5
160 million years ago) further sculpted this valley system by overriding the Niagara Escarpment and
161 excavating most deeply in the shale at the eastern end of the lake, moderately deeply in the shales

162 of the central portion, and least deeply in the limestone/dolomite bedrock at the western end of
163 the lake, a process that formed three distinctive basins (Western, Central and Eastern basins) that
164 characterize Lake Erie (Herdendorf, 2013). After the most recent glacial advance (Wisconsinan
165 Stage), the ice margin receded in pulses, with several ridges of glacial debris (moraines) being
166 deposited under what is now the bed of Lake Erie (Lewis et al. 2012). Moraines composed
167 mainly of glacial till clay and gravel were built up at the ice margins as advancing or retreating
168 ice sheets paused, which dammed earlier drainage systems at different locations. (Herdendorf and
169 Krieger 1989). The age of the bedrock units in this coastal region ranges from the Silurian Period
170 (416 to 435 million years ago) in western Ohio to the Pennsylvanian Period (307 to 318 million
171 years ago) in the bedrock highland areas (see Figure S1) (ODNR, 2018). Along the Lake Erie
172 shore west of Sandusky, bedrock units exposed at the surface or buried beneath glacial deposits
173 are mostly Silurian and Devonian-age limestone and dolomite (exposed at Catawba, Bass, and
174 Kelleys Islands). East of Sandusky, Devonian-age shale trends along the shore into northeastern
175 Ohio (exposed in the valley walls of the Vermilion, Black, and Rocky Rivers).

176 The soil parent materials, which refer to the underlying mineral or organic materials from which
177 soil forms, are usually categorized by means of sediment transport e.g., ice, water, wind, and
178 gravity. Myers et al. (2000) and ODNR (2018) classified the soils across the three study sites into
179 Lakebed (lacustrine) soils and glacial till soils based on their parent materials. The Lakebed soils
180 are fine-textured lacustrine deposits usually formed at the lake bottoms and were deposited
181 during the prehistoric stages of Lake Erie's formation (ODNR, 2018). Glacial till soils are
182 unsorted (variable-sized) materials that were mixed, crushed, compressed, and transported by the
183 movement of glaciers. Till soils have variable textures and can be slightly permeable below the

184 surface. Also, these soils can be classified further into Inceptisols, Alfisols, mollisols, and a small
 185 fraction of Entisols based on the dominant soil order (see Figure S2).



186
 187 **Figure 1.** Map of the United States (top left), surficial geologic map of the study area showing
 188 the dominant soil parent material overlaid on hillshade basemap (right). Data source: Gridded
 189 Soil Survey Geographic Database for Ohio (SSURGO, 2012), with dominant soil parent material
 190 overlay by S. Subburayalu and B. Slater (2013).

191 3. Materials and methods

192
 193 **3.1. Lithostratigraphy**
 194 2 inch diameter piezometers were installed at the upland, transition, and wetland zones of each of
 195 the three field sites, using a hand auger with soil samples retrieved every 0.1 m. The piezometers
 196 were deeper at the upland zones terminating at about 6 m, while the transition and wetland
 197 piezometers terminated at about 2 m and 1 m, respectively. The soil samples retrieved during

198 piezometer installation were used to create lithostratigraphic logs that were used to ground-truth
199 some of the geophysical measurements.

200 **3.2. Electromagnetic Induction**

201 The EMI method measures the response of the ground to the propagation of Electromagnetic
202 fields made up of an alternating electric intensity and magnetizing force. An alternating current is
203 passed through a transmitter coil (a loop of wire) placed over the ground to generate a primary
204 (inducing) magnetic field which spreads out both above and below the ground surface. In a
205 homogeneous ground, the primary field is detected by a receiver coil with a minor reduction in
206 amplitude (Haldar, 2018). In the presence of a conducting body, however, the magnetic
207 component of an electromagnetic field penetrating the ground induces the flow of eddy currents
208 within the conductor. The eddy currents generate their own secondary electromagnetic field,
209 which differs in phase, amplitude, and direction, sensed by the receiver coil. The differences
210 between transmitted and received electromagnetic fields reveal the presence of a conductor and
211 provide information on its geometry and electrical properties (Geonics, 2009; Gebers et al. 2009).
212 For this study, EMI data was acquired with an EM38-MK2 sensor (Geonics, Canada). The sensor
213 consists of a transmitter and two receiver coils at separation distances of 0.5 m and 1.0 m from
214 the transmitter and outputs apparent electrical conductivity (ECa) at average depth ranges of 0-
215 0.75 m and 0-1.5 m in vertical mode and 0-0.38 m and 0-0.75 m in horizontal mode. However,
216 the true penetration depth of the sensor depends on the sensor frequency and conductivity of the
217 topsoil, which is site-specific (e.g., Paton, 2012). The sensor operates at a frequency of 14.5 kHz
218 and delivers ECa values in mS/m.

219 In this study, the EM38-MK2 sensor was used in vertical mode to pace around each site with a
220 back-mounted real-time kinematic differential ground positioning system (RTK-DGPS). The

221 RTK-DPS system was set up using two Emlid Reach RS2+ differential GPS (Emlid Ltd., Hong
222 Kong), one was fixed at a location that serves as the base while the other was mounted on a
223 backpack and serves as the rover, this allowed the acquisition of a georeferenced data at about 0.3
224 m accuracy. The data acquisition was monitored real-time using EM38-MK2win data logging
225 system operated on a Windows 10 based field tablet computer. The EMI system was nulled and
226 calibrated at each site before data acquisition, and the sensor was held up at about 0.4 m from the
227 ground during acquisition. The acquired ECa data was interpolated with Surfer 12 (Golden
228 Software, Colorado, USA), using inverse distance to a power approach (Franke, 1982), resulting
229 in a spatially distributed ECa. At the CRC transition and wetland zones, measurements were
230 repeated in December 2022 and April 2023 to investigate the temporal variability of the soil ECa.

231 **3.3. Electrical resistivity tomography**

232 Electrical resistivity tomography is used to determine the subsurface distribution of electrical
233 resistivity by carrying out a set of resistance measurements on the ground surface and/or in
234 boreholes. Current is injected into the ground via two current electrodes, and the resulting
235 potential difference is measured at another two electrodes using different combinations of current
236 and potential electrodes along a transect or grid. A geophysical inversion of the acquired data is
237 then performed to obtain the resistivity of the subsurface (see Loke, 2000). In this study, ERT
238 data were collected across the three sites with a SuperSting R8 resistivity meter and an 84-
239 electrode switch box (Advanced Geosciences Inc., Austin, TX), using the dipole-dipole electrode
240 configuration (e.g. Loke, 2000) and 1 m unit electrode spacing. The data was collected in
241 automatic mode, which automatically records resistivity data using a preprogrammed command
242 file and the distributed Swift automatic multi-electrode system (AGIUSA, 2005). At the CRC
243 site, ERT data were collected along 3 transects in the upland zone and another 3 transects
244 between the transition and wetland zones. At the PTR site, six different transects were used to

245 acquire ERT data. The two longest profiles were acquired using a roll-along method up to a total
246 spread of 147 m from the transition zone to the wetland zone, and 168 m from the upland zone to
247 the wetland zone, while the other four transects were 84 m long. The ERT data at the OWC site
248 were acquired along 7 different transects cutting across the three zones, thus, a total of 19
249 resistivity profiles were obtained across the three sites. The ERT survey was designed in such a
250 way as to enable a correlation of electrical resistivity with the lithostratigraphic logs obtained
251 from the piezometers installed in each of the sites. The inversion of the acquired resistivity data
252 was performed with the AGI EarthImager 2D (Advanced Geosciences Inc., Austin, TX) using
253 smoothness constrained inversion method. Finally, the Earth Imager was used to trim the ERT
254 profiles to a depth suitable for high-resolution correction to be made with the well logs.

255 **3.4. Ground penetrating radar**

256 Ground penetrating radar is a geophysical method that uses propagating electromagnetic waves to
257 investigate the shallow subsurface based on its response to changes in the electromagnetic
258 properties of the shallow subsurface. The propagation wave velocity is determined by the relative
259 permittivity contrast between different soil layers or the background material and anomalous
260 body (e.g., Baker et al., 2007). The transmitter component of the GPR system propagates the
261 electromagnetic wave through the earth material and the interactions with the earth material
262 response are sensed by the receiver component. The GPR survey in this study was carried out on
263 short survey lines, collocated on some of the ERT survey lines in each site to allow the
264 comparison of both methods in terms of suitability for investigating vertical variations and
265 delineating subsurface heterogeneity at the land-lake interface. GPR data were collected using
266 PulseEKKO GPR system (Sensors & Software Inc., Canada) with a 200 MHz antenna.
267 Transmitter and receiver separation of 0.5 m was used, and the GPR data was collected at 0.5 m

268 intervals using a manual trigger method. The new DVL-500 ruggedized display unit (a high-
269 visibility touchscreen) was used to visualize the data simultaneously during acquisition.

270 The acquired data were processed using Sensor & Software's EKKO_Project, following standard
271 GPR processing for subsurface characterization (e.g., Annan, 2009), to remove low-frequency
272 noise due to inductive coupling effects and /or dynamic range limitations of the antennas (Annan,
273 2009).

274 **3.5. Soil and groundwater measurements**

275 Teros 12 soil sensors, which measure soil moisture, temperature, and electrical conductivity
276 (Meter Group, Inc. USA), were installed at 10 and 30 cm depth in the upland (n=4 and 2,
277 respectively), transition (n=4 and 2, respectively), and wetland (n=2 and 2, respectively) zones of
278 each site and were used to monitor monthly soil moisture (SM) changes between March 2022 and
279 April 2023.

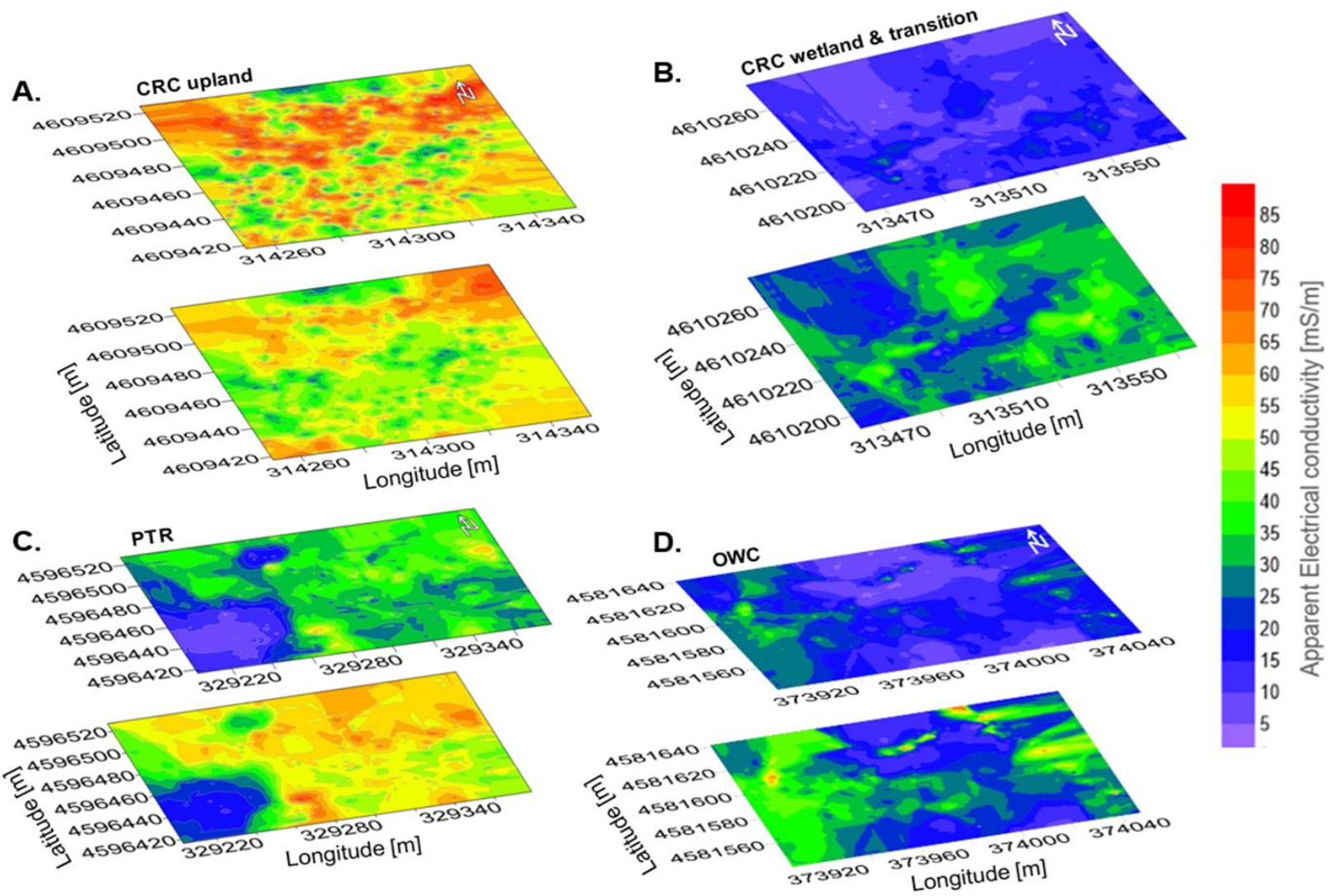
280 Also, each piezometer was instrumented with Aqua TROLL 600 multiparameter sondes (In-situ
281 Inc. USA), which were used to measure monthly changes in groundwater level and specific
282 conductivity. The sensors were equipped with wipers to minimize fouling of sensor heads and
283 calibrated according to manufacturer protocols during maintenance visits. The soil and
284 groundwater sensors were both set to log data on a 15-minute frequency.

285 **4. Results**

286 **4.1. Spatial variability of soil properties from apparent electrical conductivity**

287 The range, mean, and variance of soil apparent electrical conductivity (ECa) measured at the
288 three sites are described in Table 1. The sites show high spatial variability in the ECa distribution
289 from the 0.5 m and 1.0 m sensor separation, corresponding to average depths of 0-0.75 m and 0-
290 1.5 m, respectively (Figure 2). Also, the ECa values showed Gaussian distribution across all sites,

291 with higher values in the wetland and transition zones than the upland zones for the PTR and
292 OWC sites. The CRC upland showed higher ECa values at 0.5 m (mean = 55.3; variance = 0.041)
293 and 1.0 m (mean = 49.3; variance = 0.012) sensors separation than the CRC transition and
294 wetland at 0.5 m (mean = 12.8; variance= 0.004) and 1.0 m (mean = 28.7; variance = 0.006)
295 sensors separation. The ECa values across the sites are generally higher at the 1.0 m coil
296 separation than at 0.5 m (see Table 1), but again the CRC upland showed an opposite behavior
297 with higher ECa values at the 0.5 m sensor separation (Figure 2a, Table 1)). The CRC transition
298 and wetland zones also showed lower ECa values compared to OWC and PTR wetland and
299 transition zones.



300

301 **Figure 2.** Apparent electrical conductivity (ECa) distribution maps of the sites (a) CRC upland, (b) CRC wetland and transition, (c)
302 PTR, and (d) OWC, at transmitter-receiver spacing of 0.5 m (top) and 1.0 m (bottom) which correspond to approximate depth of 0-
303 0.75 m and 0-1.5 m respectively.

304 **Table 1** The ECa distribution across the study sites at 0.5 m and 1.0 m coil spacing

Site	ECa distribution at 0.5 m coil separation [mS/m]	ECa distribution at 1.0 m coil separation [mS/m]	Comments
CRC upland	Range: 4.5 - 85 Mean: 55.3 Variance: 0.041	22.7 - 77.9 Mean: 49.3 Variance: 0.012	- ECa is higher and more variable at top 0.5 m coil spacing - Higher ECa values than the other uplands
CRC wetland and transition	Range: 1 - 36.7 Mean: 12.8 Variance: 0.004	Range: 7.2 - 53.4 Mean: 28.7 Variance: 0.006	- ECa is higher and more variable at 1.0 m spacing
PTR	Range: 2.6 - 63.8 Mean: 31.2 Variance: 0.17	Range: 12.9 - 77 Mean: 49.4 Variance: 0.020	- ECa is higher and more variable at 1.0 m coil spacing - Lower ECa values in the upland
OWC	Range: 2 - 52 Mean: 17.9 Variance: 0.17	0.9 - 85 Mean: 27.9 Variance: 0.19	- ECa is higher and more variable at 1.0 m coil spacing - Lower ECa values in the upland

305

306

307 **4.2. Soil ECa patterns compared to traditional soil maps**

308 Previous works have recommended that ECa maps be used to optimize soil mapping (e.g.,

309 Corwin and Lesch, 2003; Mertens et al. 2008). Soil ECa maps are compared to traditional soil

310 maps from the United States Department of Agriculture (USDA), as shown in Figure 3. A closer

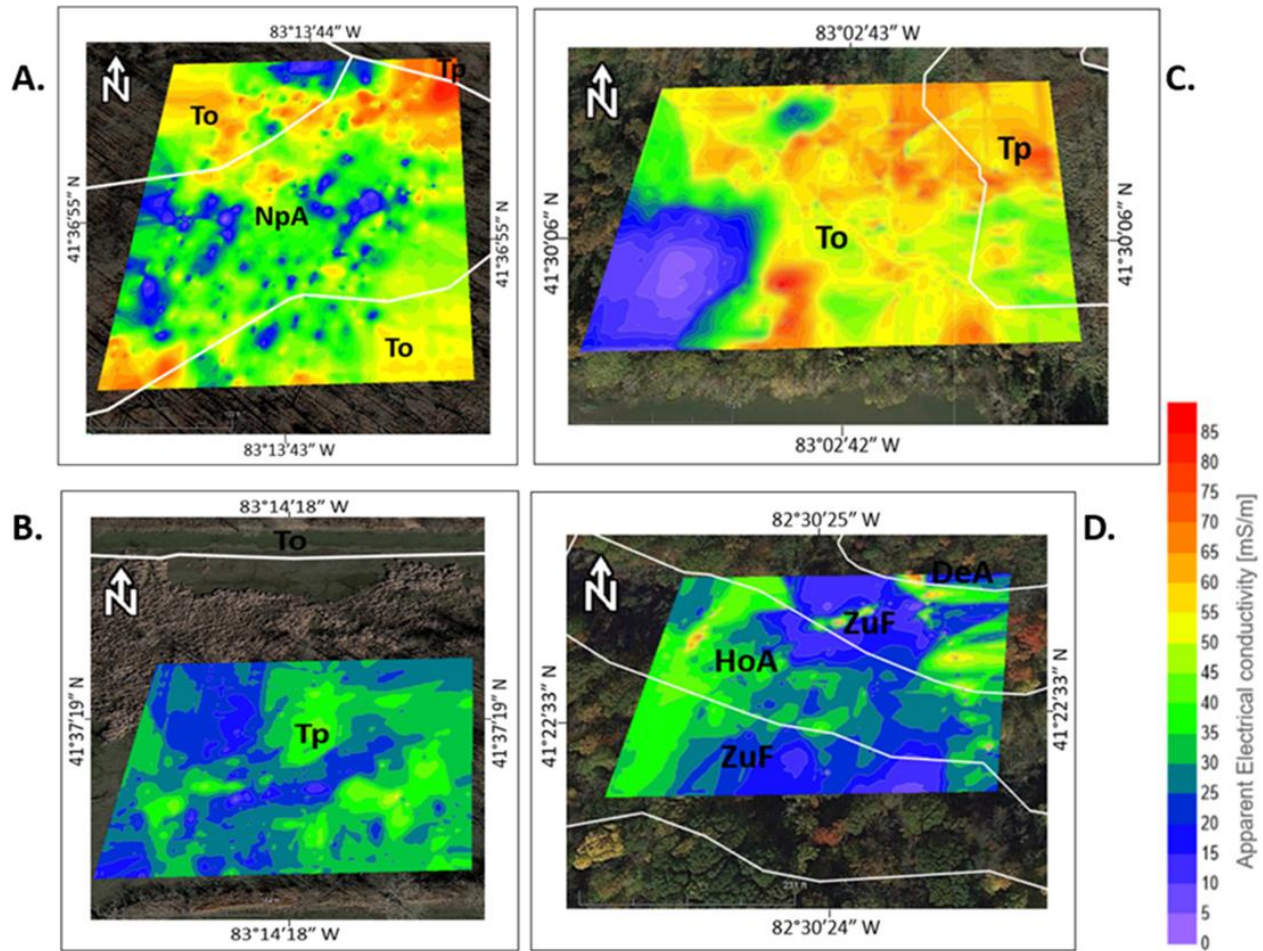
311 match between the USDA soil maps and the soil ECa maps was observed at CRC upland and

312 OWC sites than for PTR and CRC wetland and transition. Generally, the ECa maps revealed soil

313 units that were identified from the USDA soil maps, and also revealed the presence of minor

314 subunits that were not captured in the traditional soil maps (Figure 3). At the CRC site, Toledo

315 silty clay (*To*), Toledo silty clay, ponded (*Tp*) and Nappanese silty clay loam (*NpA*) were the
316 three major soil units identified from the USDA soil map (Figure 3a), both *To* and *Tp* are hydric
317 soils with 0-1 % slope while *NpA* is a non-hydric soil with 0-3 % slope. The hydric soil units *Tp*
318 and *To* showed higher ECa values than the non-hydric *NpA* soil unit. The ECa maps provided a
319 more precise detail of the lateral extension of each of these soil units than the soil map and
320 identified additional subunits that were missing in the soil map (see supplementary Table 1). At
321 the CRC wetland and transition, the USDA soil map placed the site in one soil unit (*Tp*), while
322 the ECa map showed a clearer lateral variation indicating the presence of additional units/sub-
323 units (Figure 3b). The PTR soil map showed only the *To* and *Tp* soil units (Figure 3c), with the
324 ECa values higher in *Tp* than the *To*, as was also the case at CRC upland site. The ECa map at the
325 PTR site showed a more precise lateral extent of the *Tp* and *To* soil units and also indicated the
326 presence of additional units/sub-units which were missed out in the soil map (supplementary
327 Table 1). At OWC, the soil map showed three distinct soil units which were clearly identified by
328 the ECa maps (Figure 3D), the Zurich silt loam (*ZuF*), which is rated non-hydric with 25-40%
329 slope, Holly silt loam (*HoA*) which is rated hydric with 0-1 % slope (Hurt and Vasilas, 2006), and
330 Del Rey silt loam (*DeA*), a nearly level and somewhat poorly drained soil with 0-2 % slope. The
331 hydric *HoA* soil unit showed higher ECa values than the non-hydric units.



332

333 **Figure 3.** An overlay of soil ECa distribution from 1.0 m spaced sensors on USDA soil maps. (a-
 334 b) CRC upland and CRC transition and wetland showing three soil units; Toledo silty clay (To),
 335 Toledo silty clay, ponded (Tp) and Nappanese silty loam (NpA). (c) PTR showing two soil units;
 336 Toledo silty clay (To) and Toledo silty clay, ponded. (d) OWC showing three soil units, Zurich
 337 silt loam (ZuF), Holly silt loam (HoA) and Del Rey silt loam (DeA).

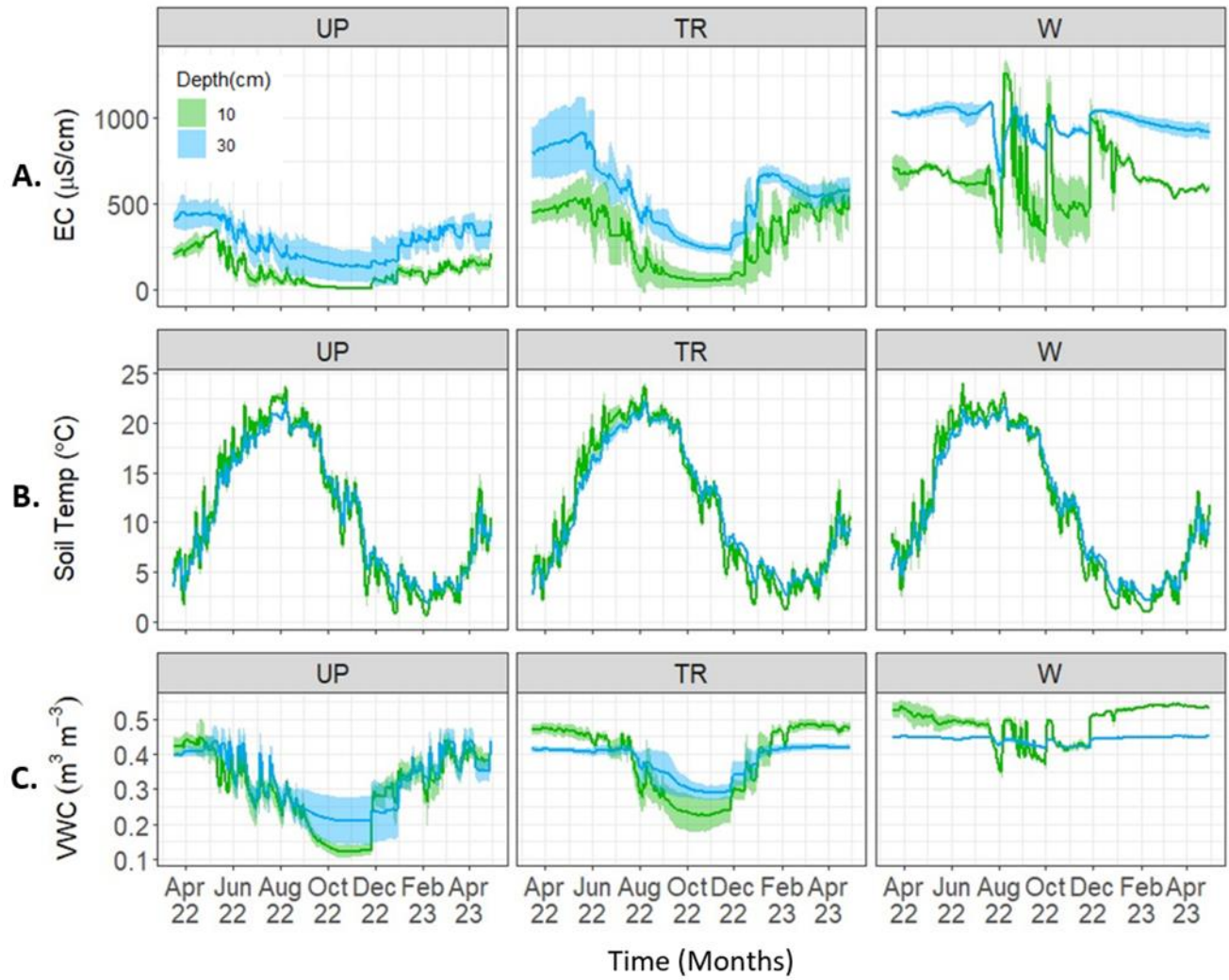
338 4.3. Soil moisture and groundwater dynamics

339 Figure 4 shows the in situ Soil moisture, temperature, and electrical conductivity (EC) data
 340 obtained from the CRC upland, transition and wetland zones. At the wetland zone, the SM
 341 increased slightly from 0.52-0.55 $m^3 m^{-3}$ at 10 cm depth, and from 0.45-0.46 $m^3 m^{-3}$ at 30 cm
 342 depth between December 2022 and April 2023. At the transition zone, the SM also increased
 343 between December 2022 and April 2023, and the values ranged from 0.26-0.32 and 0.46-0.50

344 m^3m^{-3} at 10 cm depth, and from 0.30-0.40 and 0.41-0.44 m^3m^{-3} at 30 cm depth (Figure 4c). The
345 changes in soil moisture were much more variable at the top 10 cm. During the same period, we
346 recorded a substantial increase in soil electrical conductivity from about 10-750 $\mu\text{S}/\text{cm}$ and 500-
347 1000 $\mu\text{S}/\text{cm}$ in the transition and wetland zones, respectively (Figure 4a), the soil temperature
348 was also close to 0°C as shown in Figure 4b.

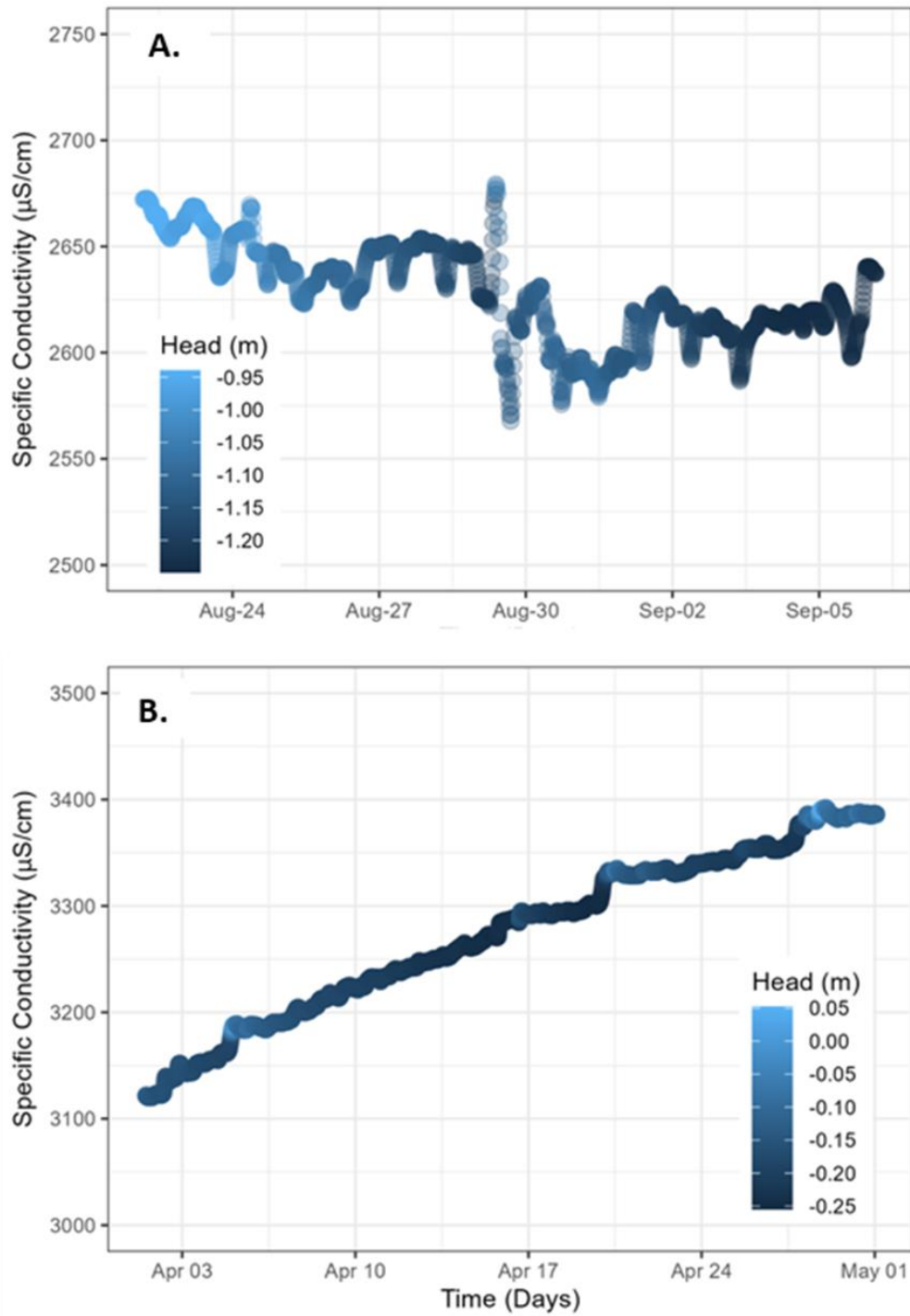
349 The specific conductivity of groundwater at the CRC transition zone from August to September
350 2022 and from April-May 2023 is shown in Figures 5a and 5B, respectively. In August 2022, the
351 specific conductivity decreased with the hydraulic head (Figure 5a). The water level in the
352 piezometers continued to decrease until it dried up in October-December 2022 (no data
353 recorded). In the same period, our results show a decrease in both soil moisture (Figure 4c) and
354 soil electrical conductivity (Figure 4a), while the soil temperature increased from April and
355 peaked in August before decreasing to a minimum around December for both transition and
356 wetland zones (Figure 4b). In April 2023, the specific conductivity showed a steady increase with
357 the hydraulic head (Figure 5b).

358



359

360 **Figure 4.** (a) Soil electrical conductivity (EC), (b) temperature and (c) moisture changes recorded
 361 between April 2022 and April 2023 at CRC upland zone (UP), transition zone (TR) and wetland
 362 zone (W).



363
364 **Figure 5.** Specific conductivity and hydraulic head variations recorded in (a) August 2022 and
365 (b) April 2023, at the CRC transition zone.

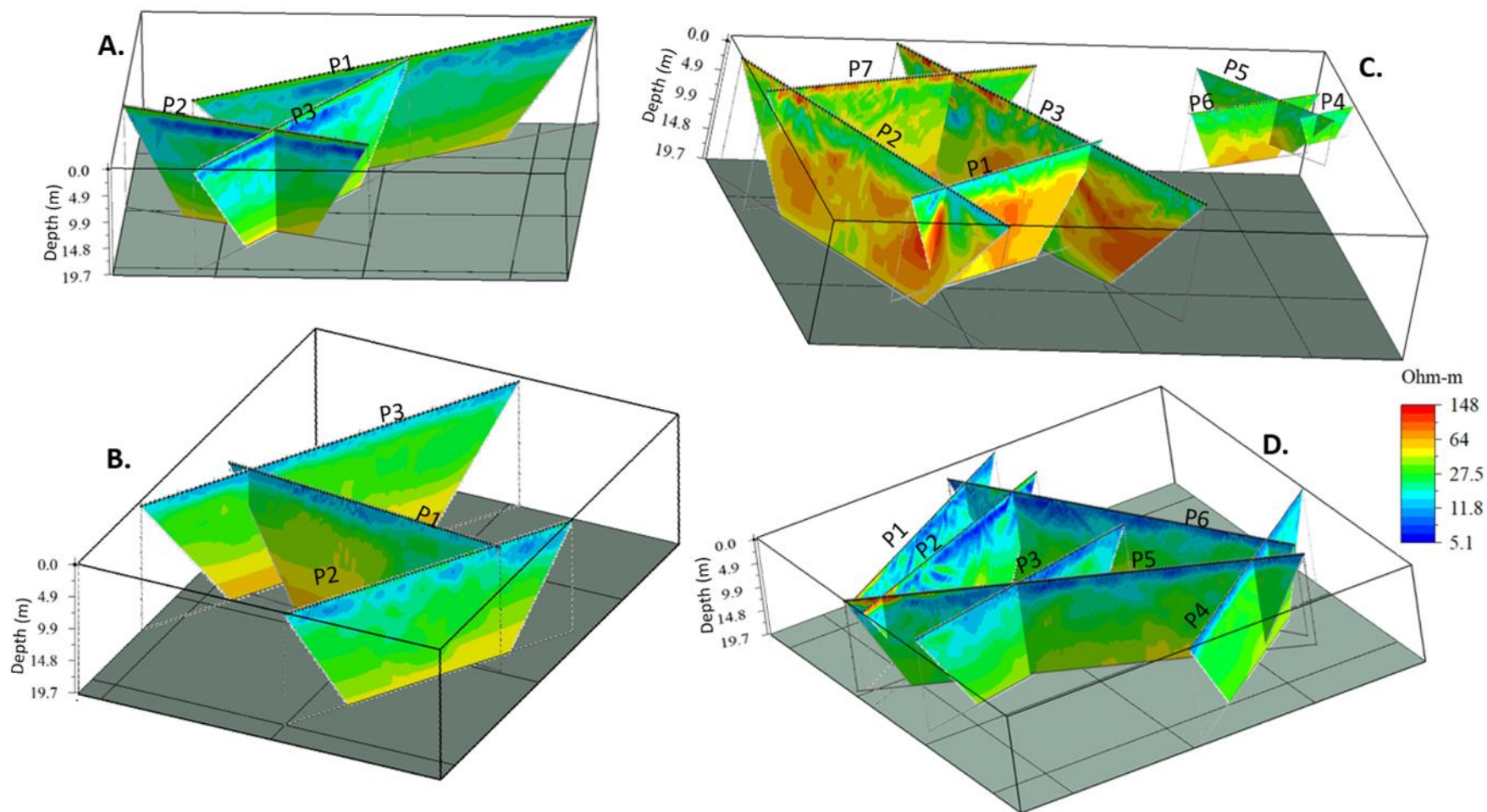
366

367 **4.4. Vertical variability of soil properties assessed from ERT and GPR**

368 The ERT results show a vertical variation in electrical resistivity, generally increasing from the
369 soil surface to 19.7 m across the three sites, as shown in Figure 6. The CRC site showed
370 resistivity values that ranged from 5.1-54.4 Ωm and 10.4-70 Ωm for the upland and wetland-
371 transition zones, respectively (Figure 6 a-b). A low resistivity layer is clearly visible at the depth
372 of 1.3-6 m in the upland and 0-3 m in the transition and wetland zones. At the PTR site, the
373 resistivity ranged from 5.5-74 Ωm (Figure 6d), with low resistivity values from the soil surface to
374 a depth of about 6 m in the transition zone and about 3 m in the wetland zone. In the upland zone,
375 higher resistivity values are observed from 0-1.6 m depth. The OWC showed a more variable
376 resistivity response, which ranged from 10.2-148 Ωm (Figure 6c), high resistivity values were
377 observed in the upland but also in the transition and wetland at shallower depths compared to the
378 CRC and PTR sites. While the CRC and PTR sites are generally flat, the OWC site shows
379 significant elevation differences between the upland zone and the wetland or transition zone. The
380 ERT profiles 2 and 3, which extended from the wetland into the upland, were corrected for
381 terrain effect during inversion.

382 At the CRC transition (Figure 7a), three distinct stratigraphic layers were identified from the GPR
383 reflection radargram. Layer 3 showed stronger reflection compared to layers 1 and 2. Similarly,
384 three stratigraphic layers were also identified at the PTR site, on a transect which extended from
385 the upland zone to the wetland zone (Figure 7b). There is a visible lateral change in GPR
386 reflection at about 45 m mark along the profile, which signifies the boundary between upland soil
387 (1) and wetland soil (2) as described in Figure 7b. There are also some vertical features that
388 appeared at 10 m and 60-70 m along the profile and extended to an estimated depth of about 3-
389 3.5 m, which are probably a strong reflection of till, as the soil samples retrieved from piezometer
390 installation in this zone confirmed that the till here is very rich in pebbles (diamictites) composed

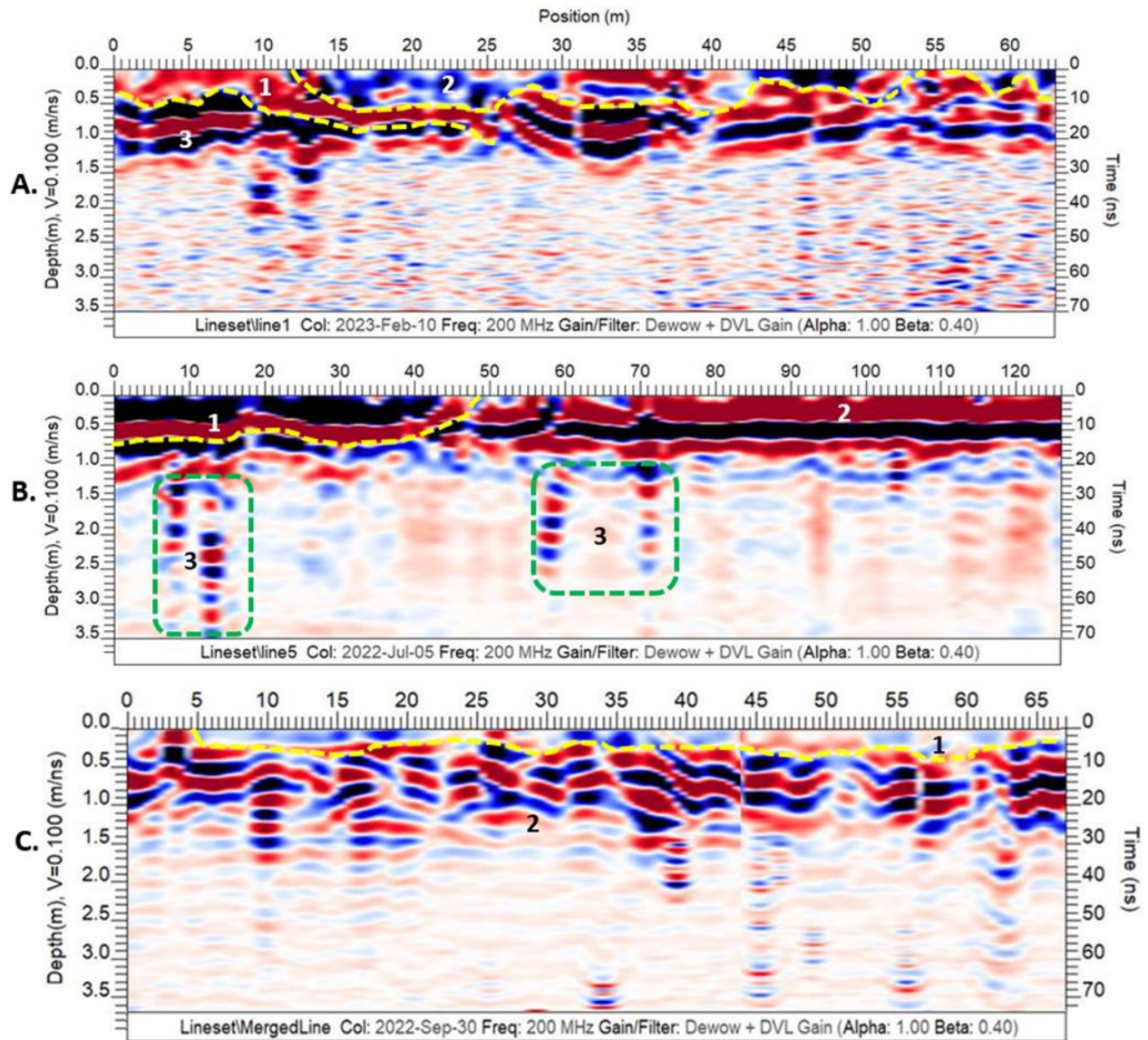
391 mainly of black shale. At the OWC site, two distinctive layers were observed. A top layer (1) of
392 about 0.5 m thickness which showed a weak reflection and a second layer (2) with a stronger
393 reflection which lies between 0.5-1.5 m. The GPR data is useful to identify the stratigraphic
394 boundaries at these sites but does not reveal what the structures are. Combining different
395 geophysical methods is useful to overcome this challenge by leveraging the strength of each
396 method to bridge the gap in interpretation where other methods are lacking. Thus, the GPR
397 results will be compared with other methods to better identify the observed layers and structures
398 (see section 4.6).



399

400 **Figure 6.** Electrical resistivity tomography profiles from the sites. (a) CRC upland (b) CRC transition and wetland (c) OWC site (d)

401 PTR site. For clarity, the profiles in each zone are numbered as P1, P2...Pn., according to the sequence of acquisition.

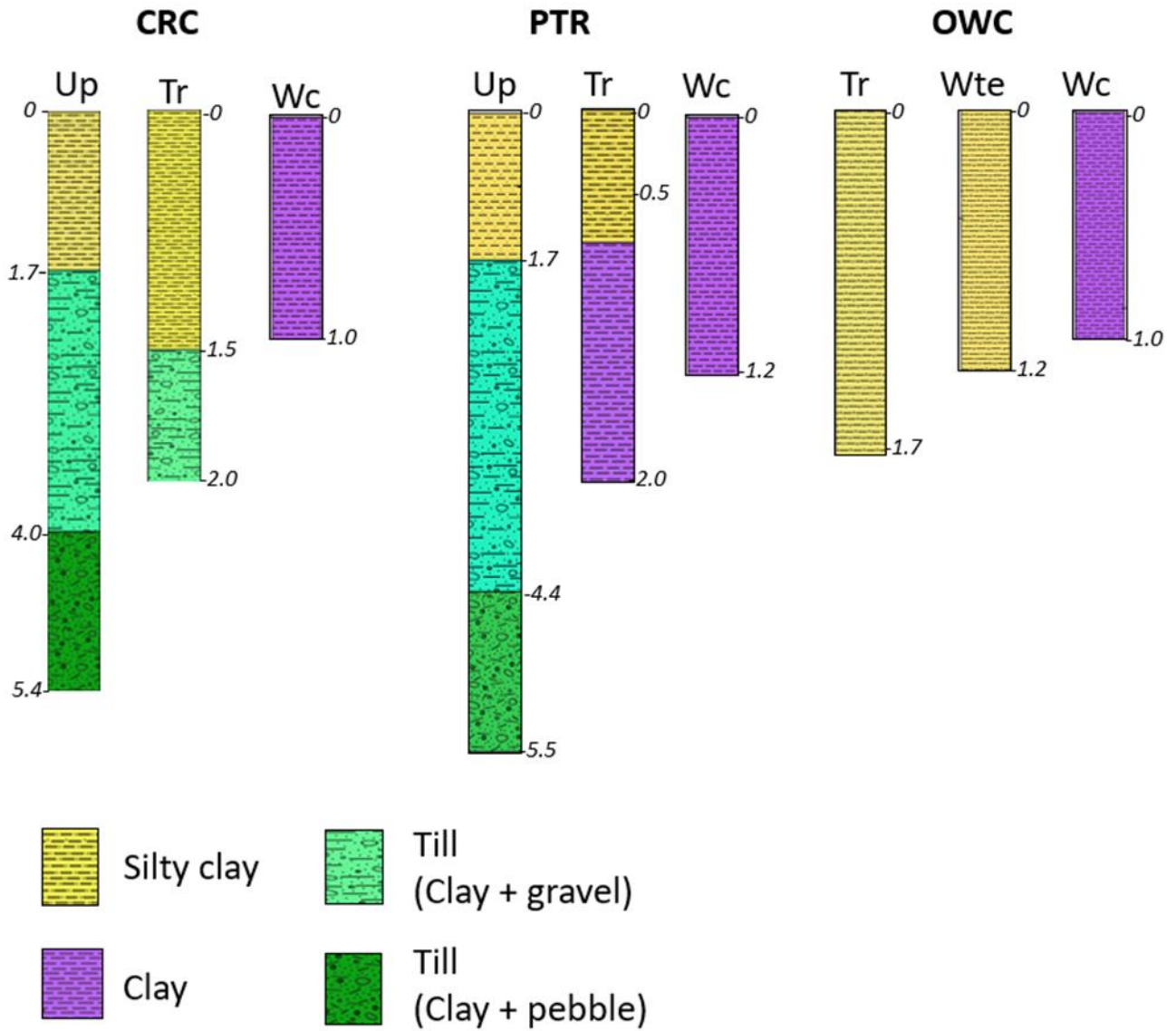


402
 403 **Figure 7.** Ground penetrating radar profiles from the sites (a) CRC transition zone (b) PTR
 404 upland to wetland zone (c) OWC wetland edge to wetland center. The numbers on the figures
 405 indicate the different layers identified from the GPR reflection, while the yellow and green lines
 406 are used to mark the layer boundaries.

407
 408 **4.5. Lithostratigraphy reconstructed from well logs**

409 The lithostratigraphy of the three sites is described here based on the borehole logs obtained from
 410 the upland, transition, and wetland zones of each site (Figure 8). The CRC and PTR upland zones
 411 are characterized by silty clay layers at the top 1.7 m, underlain by clay with intercalations of

412 black shale and claystone (glacial till) which extends down to 5.5 m. The CRC transition zone
413 shows similar stratigraphy with the CRC upland, while the PTR transition zone is different from
414 the upland, it shows a layer of silty clay which extends down to 0.5 m followed by a clay layer
415 down to 2 m. The OWC upland zone is characterized by a thin layer of silty loam at the top 6 cm,
416 followed by a clay layer extending down to 1.35 m, then a silty clay from 1.35 to 4.0 m, followed
417 by water-saturated clay from 4-5.8 m. The wetland zones of the three sites show similar
418 stratigraphy characterized by a 1 m thick clay layer.



420
421

422 **Figure 8.** The lithostratigraphy of the sites described based on borehole logs from the upland
 423 zones (Up), the transition zones (Tr), wetland edge (Wte) and wetland center (Wc) of the three
 424 sites, with depth in meters.

425 **4.6. Combining ERT, lithological logs and GPR**

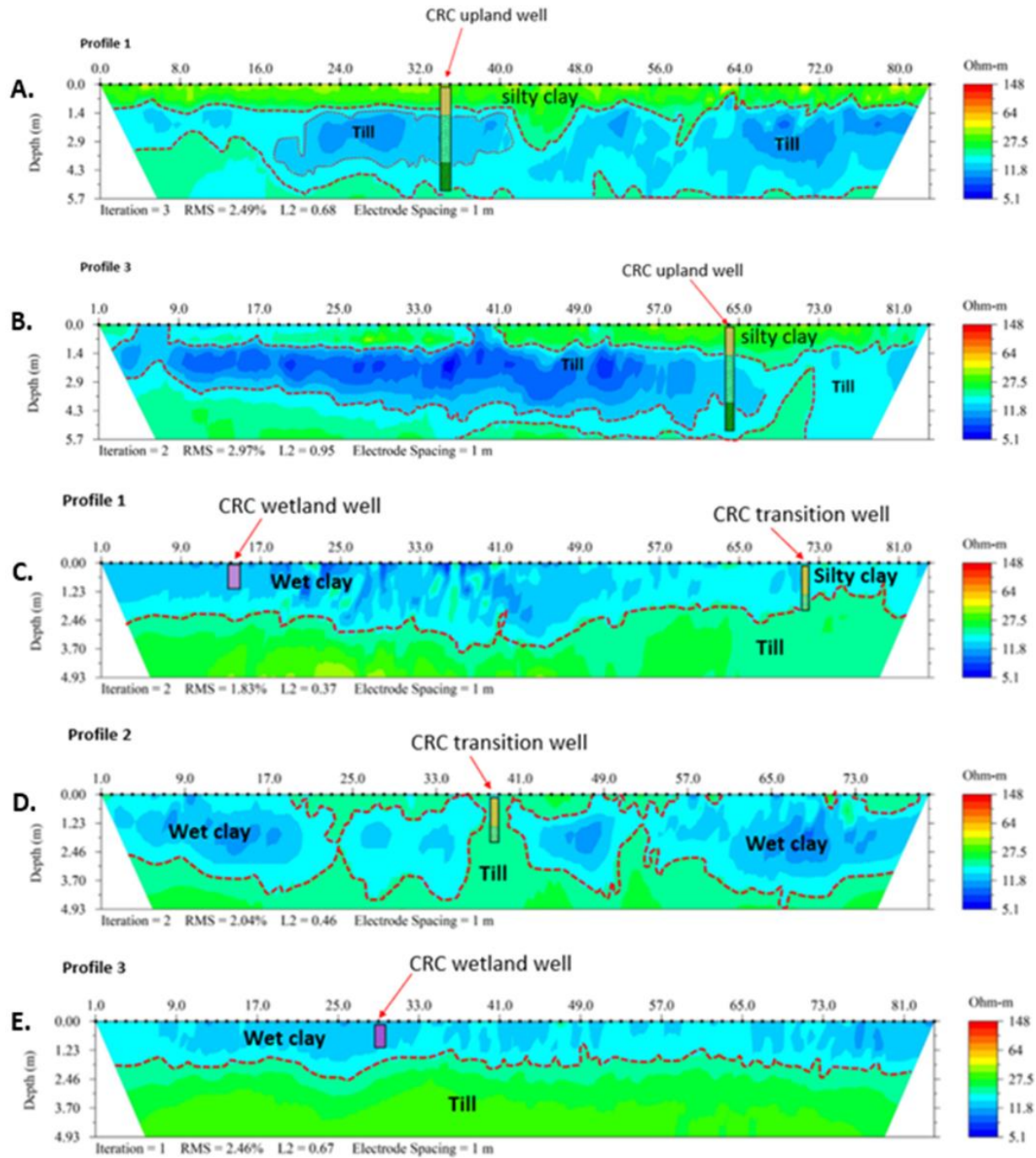
426 At the CRC site, the upland well was correlated with two ERT profiles that cut across the well at
 427 different positions (Figure 9a-b). The stratigraphic boundaries observed in the well-log matched
 428 that of the ERT profiles. The well log identified a sharp boundary in the till layer marked by a

429 different clay-to-rock fragment ratio; this boundary was also observed in the ERT profiles (Figure
430 9a-b). The low resistivity layer in the upland is tied to the till, while the higher resistivity layer is
431 tied to the silty clay layer. In the transition and wetland zones, the stratigraphic boundaries
432 observed in the wells also matched that of the ERT profiles taken across them (Figure 9c-e).
433 Figure 9c showed a transect from the wetland zone to the transition zone, the well log and ERT
434 result identified a shift from clay-dominated top layer in the wetland to silty clay-dominated top
435 layer in the transition zone. The Till layer appeared deeper in the wetland zone (Figure 9e)
436 compared to parts of the transition zone (Figure 9d).

437 At the PTR site, the upland well log was tied to two ERT profiles (Figure 10a and 10d). The
438 stratigraphic boundaries observed from the well log also matched that of the ERT profiles very
439 closely; the high resistivity layer observed from the ERT profile was confirmed to be a layer of
440 dry silty clay. The transition well log was tied to an ERT profile that ran from the upland zone
441 into the transition zone (Figure 10b) and another that ran from the transition zone into the
442 wetland zone (Figure 10e). The top layer of silty clay identified from the well log clearly matched
443 the ERT result. In the wetland zone, both the ERT profile and the well log identified a top layer
444 of clay. Since the wetland well is just 1 m deep, it was not possible to determine the thickness of
445 this clay from the well log, but the ERT profile showed the thickness to be between 2.5-3.2 m in
446 the wetland zone.

447 At the OWC site, ERT profiles were correlated with the wells existing in the transition and
448 wetland zones. The transition zone showed relatively uniform resistivity at the top 3 m which is
449 tied to a silty clay layer based on the well log obtained at 2 m depth (Figure 11d). The wetland
450 edge also showed a less heterogeneous layer at the top 3 m which is tied to silty clay as well
451 based on well log data (Figure 11a and 11c). The wetland center showed lower resistivity

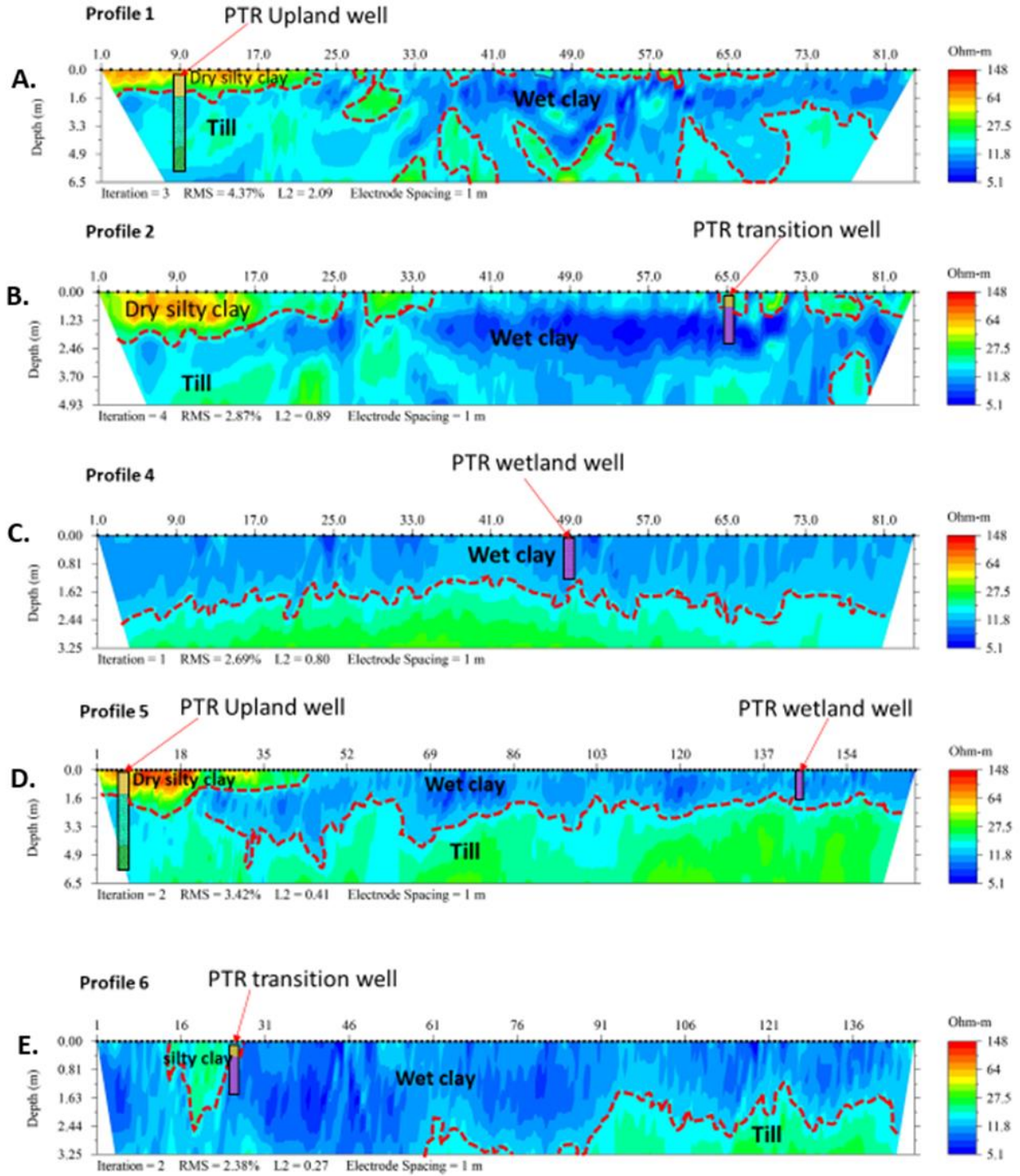
452 response compared to the transition zone, this low resistivity unit was found to be a wet clay
453 layer when tied to the well log obtained at 1 m depth (Figure 11a-b). These results indicate that
454 the stratigraphy and soil moisture dynamics are the key drivers of spatial heterogeneities at these
455 sites.



456

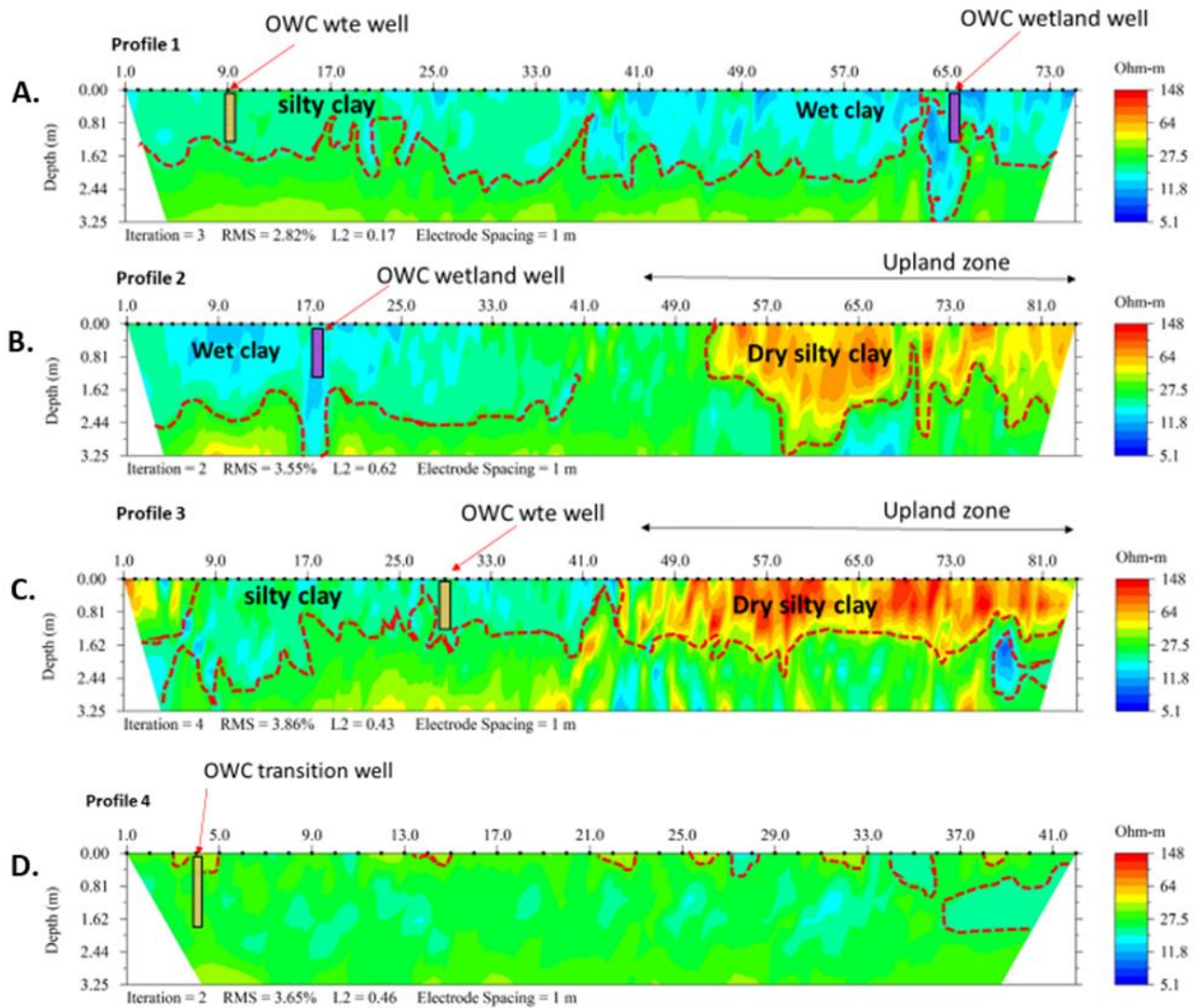
457 **Figure 9.** Correlation of well log and ERT profiles at the Crane creek (CRC) site, showing a
458 close match between stratigraphic boundaries from well logs and that of ERT. (a-b) The dark
459 blue and light blue layers indicate two distinct layers of till identified at CRC upland, the dark
460 blue till layer is clay-rich while the light blue is gravel-rich. (c-e) The till layer at CRC transition
461 zone is composed of more gravel than clay and thus showed higher resistivity than the
462 surrounding wet clay. The existing well at CRC wetland is not deep enough to get into the till.

463



464
 465
 466 **Figure 10.** Correlation of well log and ERT profiles at the Portage River (PTR) site. The
 467 stratigraphic boundaries observed from the well logs matched that of the ERT, showing dry silty

468 clay in the upland zone as the most resistive layer (a, b and c), and wet clay in the transition and
 469 wetland zones as the least resistive (a-e)

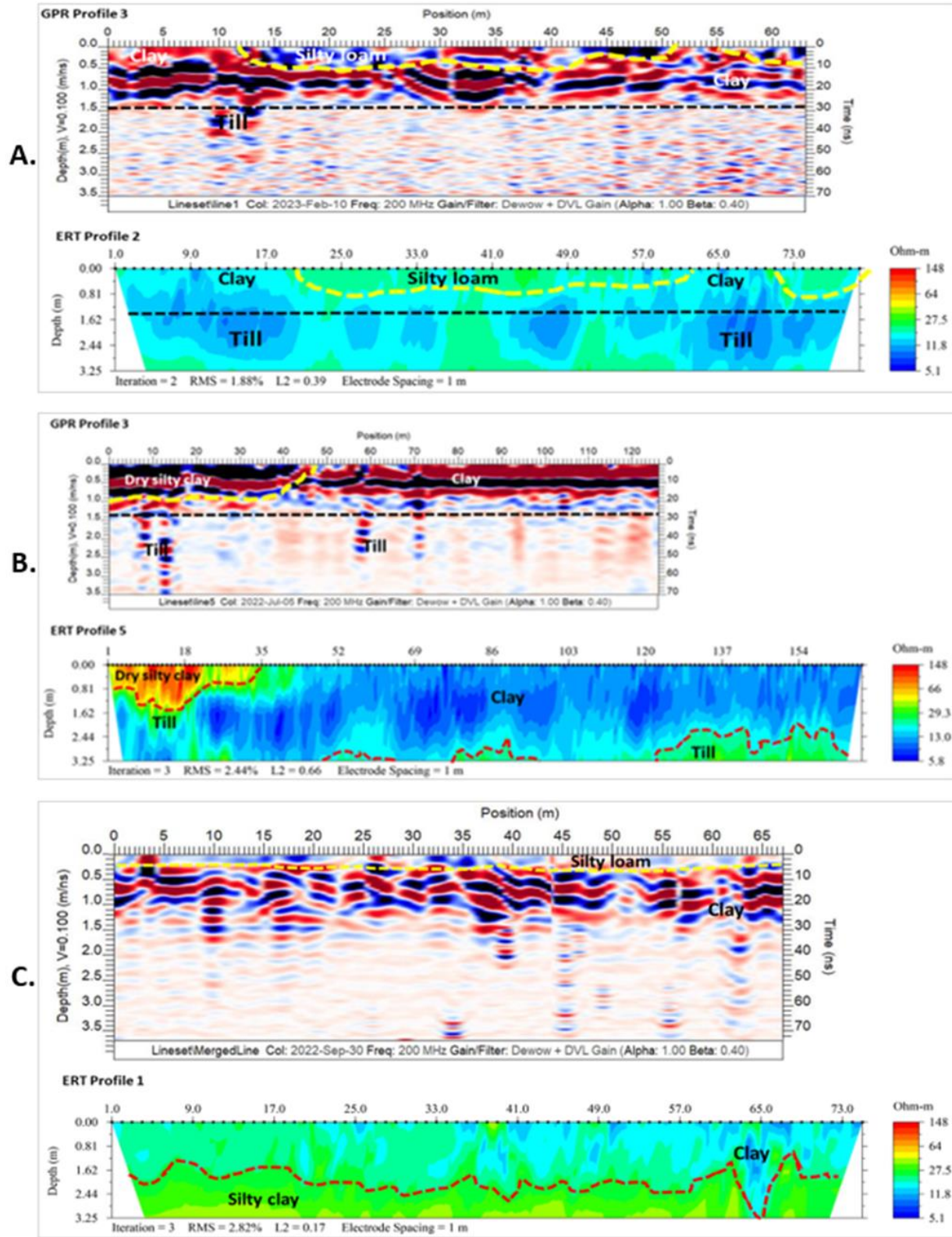


470
 471 **Figure 11.** Correlation of well logs and ERT profiles at the Old woman creek (OWC) site,
 472 showing wet clay layers in the wetland zone as the least resistive (a-b) and the dry silty clay layer
 473 in the upland as the most resistive (b-c).

474
 475 Figure 12 shows a comparison between collocated ERT and GPR profiles, it is clear that GPR
 476 also provided information about vertical variability of soil properties at the study sites. However,
 477 the GPR sensitivity at these sites is limited to the top 1.5 m, probably due to signal attenuation
 478 due to conductive losses resulting from the high clay content at these sites, while the ERT clearly

479 showed better depth resolution. Correlating the GPR results (Figure 7b) and ERT results (Figure
480 10d) was useful to confirm that the vertical features observed in the GPR just below the dry silty
481 clay are glacial Till (Figure 12b), this clearly shows that combining different geophysical
482 methods is a better approach for subsurface characterization than using one method alone.

483



484

485 **Figure 12.** Comparing collocated ERT and GPR profiles at (a) CRC transition, (b) PTR upland to
486 wetland transect, (c) OWC wetland edge to wetland center transect. Combining the GPR and
487 ERT methods helped to clearly identify the clay, silty loam, silty clay and till layers.

488 **5. Discussion**

489

490 **5.1. Spatiotemporal variation of soil properties**

491 We hypothesized that ECa will be low in the upland zones and increase as we move from the
492 upland to the transition zone, and from the transition to the wetland zone across the sites due to
493 increasing SM. The EMI results from PTR and OWC agreed with our hypothesis (Figure 2c and
494 2d), but higher conductivity was observed at the CRC upland (Figure 2a) compared to its
495 transition and wetland (Figure 2b). This is probably due to the temporal variability of SM at the
496 sites considering that the upland area is a separate plot from the wetland and transition, and the
497 EM measurements were conducted at different periods; December (upland) and April (transition
498 and wetland). When this data was compared with the monthly soil moisture data measured at the
499 sites between April 2022 and April 2023, it was seen that SM is higher in April than in December
500 (Figure 4a-b). This should have resulted in higher ECa values in April compared to December but
501 this was not the case as supplementary Figure 3 is showing the opposite. These results indicate
502 that soil moisture is the key driver of lateral variation in ECa. The EMI results also showed that
503 soil ECa varied laterally and vertically between both 0.5 m and 1.0 m sensor separations across
504 each site, which is expected. Soil aggregate properties such as proportions of sand, silt, and clay
505 are known to influence the bulk electrical conductivity of the soil (e.g. Domsch and Giebel, 2004;
506 Emmanuel et al. 2023). Soil moisture (SM), soil organic matter (OM), cation exchange capacity
507 (CEC) and salinity are all recognized as key factors that govern soil electrical conductivity. For
508 example, previous studies have found that the ECa correlates strongly with soil moisture (SM)

509 and organic matter (OM) (e.g. Molin and Faulin, 2013; Shanahan et al. 2015). A recent study by
510 Emmanuel et al. (2023) reported a strong correlation between ECa and silt proportion ($r^2 =$
511 0.761), and SM ($r^2 = 0.702$) for restored wetland soils located in Northwest Ohio. They also
512 found that SM correlated with OM, which further suggests that both parameters are somewhat
513 interdependent and thus challenging to decouple. Although some studies observed a slightly
514 stronger influence of OM on soil ECa (e.g., Shanahan et al. 2013; Emmanuel et al. 2023),
515 Domsch and Giebel (2004) argued that SM has a stronger influence on soil ECa, which is
516 probably the case in some wetlands considering that Emmanuel et al. (2023) found their strongest
517 correlation with silt content, which correlated better with SM ($r^2 = 0.660$) than with OM (0.632).

518 At our sites, it is possible that an increase in SM due to groundwater level rise could have led to
519 changes in soil water chemistry (e.g., dilution), which would have resulted in the observed
520 temporal variation of the ECa at the CRC transition and wetland zones (See Figure S3). SM
521 varies spatially both laterally across a site and vertically through the soil profile, this is well
522 described by Corwin and Lesch (2005). At these sites, SM was mostly higher at the top 10 cm
523 than at 30 cm depths across the sites except for the periods between June-December when SM
524 was higher at 30 cm (Figure 4c). This implies that the variation of ECa values between 0.5 m and
525 1.0 m sensor separation is due to variation in SM. EMI could therefore serve as a non-invasive
526 tool for monitoring soil water dynamics to understand ground water-soil water exchanges and
527 their control on biogeochemical processes at land-lake interfaces.

528

529 **5.2. Geophysics can help reconstruct subsurface stratigraphy**

530 To test the suitability of geophysical methods for characterizing subsurface stratigraphy of land-
531 lake interfaces, we investigated the sites using ERT, GPR and lithologic logs from piezometers.

532 The ERT results from the three sites (Figure 6) showed relatively lower resistivity values at CRC
533 and PTR in the range of 5.1-74 Ωm than at the OWC site (10.2-148 Ωm). Though the existing
534 wells at the OWC wetland were not deep enough to ground truth the high resistivity values
535 observed in the wetland zone, existing borehole data close to the upland area revealed the
536 presence of dry till at the depth of 50 ft (15m) that could explain the observed higher resistivity.
537 The correlation of the ERT data with lithological logs was very useful in understanding what
538 drives the vertical variation in electrical resistivity across the sites. For example, the high
539 resistivities observed close to the surface in the upland zones of PTR (Figure 10) and OWC
540 (Figure 11) sites were linked to dry silty clay. The results also indicate that similar soil types
541 could show different resistive responses at different sites depending on how their electrical
542 property compares to that of the surrounding material. For example, a layer of till showed very
543 low resistivity values at the CRC upland, while at the PTR site the same till layer appeared as a
544 relatively more resistive layer. This is because, at the CRC upland, the till is surrounded by more
545 resistive silty clay layers, while at the PTR site, the till is overlaid by wet clay layers, which is
546 much less resistive than the till layer.

547 The GPR method also revealed structural heterogeneity at the study sites; it clearly identified the
548 boundaries between silty loam and clay layers at CRC and OWC and between dry silty clay and
549 clay at the PTR sites. However, the GPR sensitivity at these sites is limited to the top 1.5 m
550 compared to ERT, which provided high-resolution depth sensitivity up to 19.7 m using a 1 m
551 electrode spacing. The poor resolution observed with GPR above 1.5 m depth could be linked to
552 signal attenuation due to high clay content. SM is known to cause signal attenuation in GPR data
553 (e.g. Huisman et al. 2003; Klotzsche et al. 2018; Agbona et al. 2021). This signal attenuation due
554 to water saturation is expected to be more pronounced in wetlands with high water residence time

555 and could also lead to temporal variations in GPR measurement due to seasonal variation in SM
556 in such wetlands.

557 The surficial geology map of the study area shown in Figure 1 indicates that the geology of the
558 area is characterized by lakebed soils (fine textured lacustrine deposits), underlain by glacial till
559 soils. This agrees with the ERT results of this study, which revealed that the stratigraphy is made
560 up of silty clay and clay layers which are lake bed soils (fine textured lacustrine deposits) and two
561 different types of till layers, differing in their composition (Figure 8), which the surficial geology
562 map revealed to be clayey Wisconsin till and loamy Wisconsin till. These tills are rich in clay,
563 which are expected to slow down infiltration and, thus, increase water residence time, which
564 could help to sustain diverse biogeochemical exchanges at these land-lake interfaces. The
565 electrical response of these TAI soils depends on whether they are dry or saturated, this explains
566 why silty clay layers are very resistive in upland areas where they are very dry (see Figure 10),
567 and also why glacial till showed lower resistivity at the CRC site (Figure 9a-b) and high
568 resistivity at PTR site (Figure 10). These results indicate that geophysical methods are useful to
569 reconstruct subsurface stratigraphy of land-lake interfaces.

570

571 **5.3. Geophysics can help improve soil mapping and sampling**

572 One of our hypotheses is that geophysical methods can be used to improve soil mapping and help
573 guide detailed soil sampling. To test this, we studied the site using EMI and then compared the
574 result with USDA soil maps. The close match between the USDA soil maps and the soil ECa
575 maps observed at CRC upland and OWC sites, indicates that the EMI is useful for soil mapping
576 and can be relied upon at sampling restricted sites. Additionally, it is important to note that the
577 ECa maps revealed additional soil units that were not identified from the USDA soil maps. The

578 soil units mapped by the USDA consist of about 5-15 % sub-units (see Table S1) which were not
579 shown in the soil maps, while the ECa maps provided a more precise detail of the lateral
580 extension of each of these soil units than the soil map, and also identified additional sub-units that
581 were missing in the soil map (Figure 3). Furthermore, the ECa maps reveal that all the hydric
582 soils across the sites (To, Tp and HoA) have high ECa values as shown in Figure 3 and Table D1
583 (see Table S1), this implies that the EMI could help soil scientists and ecologist to non-invasively
584 map the lateral extent of hydric soils. These results also emphasized the additional value of
585 combining different geophysical methods as a more useful approach to overcome technical
586 limitations associated with single methods by leveraging the strength of each method to bridge
587 the gap in interpretation where other methods are lacking as demonstrated in Figure 12.

588 **6. Conclusions**

589 This work demonstrates the advantage of combining different non-invasive geophysical methods
590 to characterize land-lake interfaces which is a complex and dynamic ecosystem, as no single
591 geophysical method is capable of capturing all the complexities of soil state and processes
592 particularly in a dynamic TAI ecosystem. The close match between ECa maps and USDA soil
593 maps, as well as the additional details provided by the ECa maps, implies that EMI is a useful
594 tool for optimizing soil mapping and could also be used to extrapolate soil properties, particularly
595 at sampling-restricted sites where only non-invasive measurements are feasible.

596 Unlike the aggregate and the pore approaches of investigating soil architecture which focuses on
597 studying limited core samples, the geophysical methods show a more detailed characterization of
598 soil spatial heterogeneity, with good lateral and vertical resolution. The EMI provided better
599 lateral heterogeneity at high resolution, while ERT and GPR provided high-resolution vertical

600 variation in the soil profile. The stratigraphy of these land-lake interfaces and their soil moisture
601 dynamics were found to be the key drivers of the observed heterogeneities. Future studies should
602 consider a detailed investigation of temporal variability of the geophysical signals coupled with
603 monitoring temporal changes in SM and soil water quality to better understand the mechanism
604 behind the temporal variation of the ECa observed here, and quantify the influence of fluctuating
605 SM and groundwater levels on the geophysical measurements.

606 **Data Availability Statement**

607 The data associated with this study (Ehosioko et al. 2023) are available in the ESS-DIVE data
608 repository: [https://data.ess-dive.lbl.gov/datasets/ess-dive-5fe23e299966ce8-
609 20231007T202450197](https://data.ess-dive.lbl.gov/datasets/ess-dive-5fe23e299966ce8-20231007T202450197)

610
611 **Acknowledgements**
612 This research is based on work supported by COMPASS-FME, a multi-institutional project
613 supported by the U.S. Department of Energy, Office of Science, Biological and Environmental
614 Research as part of the Environmental System Science Program. The Pacific Northwest National
615 Laboratory is operated for DOE by Battelle Memorial Institute under contract DE-AC05-
616 76RL01830.

617 **References**

618 Agbona, A., Teare, B., Ruiz-Guzman, H., Dobрева, I. D., Everett, M. E., Adams, T., ... Hays, D.
619 B. (2021). Prediction of root biomass in cassava based on ground penetrating radar
620 phenomics. *Remote Sensing*, 13(23), 1–18. <https://doi.org/10.3390/rs13234908>
621 AGIUSA. (2005). *Instruction Manual*. Austin, TX, USA.
622 Ameli, A. A., & Creed, I. F. (2017). Quantifying hydrologic connectivity of wetlands to surface
623 water systems. *Hydrology and Earth System Sciences*, 21(3), 1791–1808.
624 <https://doi.org/10.5194/HESS-21-1791-2017>

- 625 Annan A.P. (2009). Electromagnetic principles of ground penetrating radar. In: Jol HM (ed)
626 Ground penetrating radar theory and applications. Elsevier, Amsterdam, pp 4–38
- 627 Baker, G.S., Jordan, T.E., and Talley, J. (2007). An introduction to ground penetrating radar
628 (GPR), in Baker, G.S., and Jol, H.M., eds., *Stratigraphic Analyses Using GPR: Geological*
629 *Society of America Special Paper 432*, p. 1–18, doi: 10.1130/2007.2432(01).
- 630 Baveye, P. C., Otten, W., Kravchenko, A., Balseiro-Romero, M., Beckers, É., Chalhoub, M., ...
631 Vogel, H. J. (2018). Emergent Properties of Microbial Activity in Heterogeneous Soil
632 Microenvironments: Different Research Approaches Are Slowly Converging, Yet Major
633 Challenges Remain. *Frontiers in Microbiology*, 9(AUG).
634 <https://doi.org/10.3389/FMICB.2018.01929>
- 635 Besson, A., Cousin, I., Samouëlian, A., Boizard, H., & Richard, G. (2004). Structural
636 heterogeneity of the soil tilled layer as characterized by 2D electrical resistivity surveying.
637 In *Soil and Tillage Research* (Vol. 79, pp. 239–249). Elsevier B.V.
638 <https://doi.org/10.1016/j.still.2004.07.012>
- 639 Besson, A., Séger, M., Giot, G., & Cousin, I. (2013). Identifying the characteristic scales of soil
640 structural recovery after compaction from three in-field methods of monitoring. *Geoderma*,
641 204–205, 130–139. <https://doi.org/10.1016/J.GEODERMA.2013.04.010>
- 642 Bréchet, L., Oatham, M., Wuddivira, M., & Robinson, D. A. (2012). Determining Spatial
643 Variation in Soil Properties in Teak and Native Tropical Forest Plots Using Electromagnetic
644 Induction. *Vadose Zone Journal*, 11(4), vjz2011.0102.
645 <https://doi.org/10.2136/VZJ2011.0102>
- 646 Corwin, D. L., & Lesch, S. M. (2003). Application of Soil Electrical Conductivity to Precision
647 Agriculture. *Agronomy Journal*, 95(3), 455. <https://doi.org/10.2134/agronj2003.0455>
- 648 Corwin, D. L., & Lesch, S. M. (2005). Characterizing soil spatial variability with apparent soil
649 electrical conductivity: I. Survey protocols. *Computers and Electronics in Agriculture*, 46(1–
650 3), 103–133. <https://doi.org/10.1016/J.COMPAG.2004.11.002>
- 651 Dexter, A. R. (1988). Advances in characterization of soil structure. *Soil and Tillage Research*,
652 11(3–4), 199–238. [https://doi.org/10.1016/0167-1987\(88\)90002-5](https://doi.org/10.1016/0167-1987(88)90002-5)
- 653 Domsch, H., & Giebel, A. (2004). Estimation of soil textural features from soil electrical
654 conductivity recorded using the EM38. *Precision Agriculture*, 5(4), 389–409.
655 <https://doi.org/10.1023/B:PRAG.0000040807.18932.80/METRICS>
- 656 Doolittle, J. A., & Brevik, E. C. (2014). The use of electromagnetic induction techniques in soils
657 studies. *Geoderma*, 223–225(1), 33–45. <https://doi.org/10.1016/J.GEODERMA.2014.01.027>
- 658 Doro, K. O., Leven, C., Cirpka, O. A. (2013): Delineating subsurface heterogeneity at a River
659 Loop using geophysical and hydrogeological methods. *Environ. Earth Sci.*, 69 (2) 335 – 348
660 doi:10.1007/s12665-013-2316-0
- 661 Emmanuel, E. D., Christian, Lenhart, F., Weintraub, M. N., & Doro, K. O. (2023). Estimating
662 Soil Properties Distribution at a Restored Wetland Using Electromagnetic Imaging and
663 Limited Soil Core Samples. *Wetlands* 2023 43:5, 43(5), 1–19.
664 <https://doi.org/10.1007/S13157-023-01686-3>

- 665 Franke, R. (1982), Scattered Data Interpolation: Test of Some Methods, *Mathematics of*
666 *Computations*, v. 33, n. 157, p. 181-200.
- 667 Gebbers, R., Lück, E., Dabas, M., & Domsch, H. (2009). Comparison of instruments for
668 geoelectrical soil mapping at the field scale. *Near Surface Geophysics*, 7(3), 179–190.
669 <https://doi.org/10.3997/1873-0604.2009011>
- 670 Geonics L (2009) EM38–MK2 ground conductivity meter operating manual, Canada Ontario
- 671 Grote, K., Hubbard, S., & Rubin, Y. (2003). Field-scale estimation of volumetric water content
672 using ground-penetrating radar ground wave techniques. *Water Resources Research*, 39(11).
673 <https://doi.org/10.1029/2003WR002045>
- 674 Halder, S. K. (2018). *Mineral Exploration, principles and applications (Second Edition)*, p. 103-
675 122
- 676 Hansen, M. C. (1989). History of Lake Erie. *Ohio Geology Newsletter*.
- 677 Huisman, J. A., Hubbard, S. S., Redman, J. D., & Annan, A. P. (2003). Measuring Soil Water
678 Content with Ground Penetrating Radar: A Review. *Vadose Zone Journal*, 2, 476–491.
- 679 Hurt, G. W., & Vasilas, L. M. (2006). Field indicators of hydric soils in the United States.
- 680 Kemna, A., Binley, A., Cassiani, G., Niederleithinger, E., Revil, A., Slater, L., ... Zimmermann,
681 E. (2012). An overview of the spectral induced polarization method for near-surface
682 applications. In *Near Surface Geophysics (Vol. 10, pp. 453–468)*. EAGE Publishing BV.
683 <https://doi.org/10.3997/1873-0604.2012027>
- 684 Kessouri, P., Furman, A., Huisman, J. A., Martin, T., Mellage, A., Ntarlagiannis, D., ...
685 Placencia-Gomez, E. (2019). Induced polarization applied to biogeophysics: recent advances
686 and future prospects. *Near Surface Geophysics*, 17, 595–621.
687 <https://doi.org/10.1002/nsg.12072>
- 688 Kizhlo, M., & Kanbergs, A. (2009). The Causes of the Parameters Changes of Soil Resistivity. In
689 *Scientific proceedings of Riga Technical University* (pp. 43–46).
690 <https://doi.org/10.2478/v10144-009-0009-z>
- 691 Klotzsche, A., Jonard, F., Looms, M. C., van der Kruk, J., & Huisman, J. A. (2018). Measuring
692 Soil Water Content with Ground Penetrating Radar: A Decade of Progress. *Vadose Zone*
693 *Journal*, 17(1), 0. <https://doi.org/10.2136/vzj2018.03.0052>
- 694 Kravchenko, A., Otten, W., Garnier, P., Pot, V., & Baveye, P. C. (2019). Soil aggregates as
695 biogeochemical reactors: Not a way forward in the research on soil–atmosphere exchange of
696 greenhouse gases. *Global Change Biology*, 25(7), 2205–2208.
697 <https://doi.org/10.1111/GCB.14640>
- 698 Krüger, J., Franko, U., Fank, J., Stelzl, E., Dietrich, P., Pohle, M., & Werban, U. (2013). Linking
699 Geophysics and Soil Function Modeling–An Application Study for Biomass Production.
700 *Vadose Zone Journal*, 12(4), vzj2013.01.0015. <https://doi.org/10.2136/VZJ2013.01.0015>
- 701 Loke, M.H. (2000) *Electrical Imaging Surveys for Environmental and Engineering Studies. A*
702 *Practical Guide to 2-D and 3-D Surveys*, 61.

- 703 Maestre, F.T., Cortina, J. (2002). Spatial patterns of surface soil properties and vegetation in a
704 Mediterranean semi-arid steppe. *Plant Soil* 241, 279–291.
- 705 McBratney, A., Minasny, B., 2007. On measuring pedodiversity. *Geoderma* 141, 149e154
- 706 Mertens, F. M., Pätzold, S., & Welp, G. (2008). Spatial heterogeneity of soil properties and its
707 mapping with apparent electrical conductivity. *Journal of Plant Nutrition and Soil Science*,
708 171(2), 146–154. <https://doi.org/10.1002/JPLN.200625130>
- 709 Michot, D., Benderitter, Y., Dorigny, A., Nicoullaud, B., King, D., & Tabbagh, A. (2003). Spatial
710 and temporal monitoring of soil water content with an irrigated corn crop cover using
711 surface electrical resistivity tomography. *Water Resources Research*, 39(5).
712 <https://doi.org/10.1029/2002WR001581>
- 713 Molin, J. P., & Faulin, G. D. C. (2013). Spatial and temporal variability of soil electrical
714 conductivity related to soil moisture. *Scientia Agricola*, 70(1), 01–05.
715 <https://doi.org/10.1590/S0103-90162013000100001>
- 716 Myers, D.N., Thomas, M.A., Frey, J.W., Rheume, S.J., & Button, D.T. (2000). Water quality in
717 the Lake Erie-Lake Saint Clair Drainages Michigan, Ohio, Indiana, New York, and
718 Pennsylvania, 1996-98: U.S Geological Survey Circular 1203, 35p.
719 <https://pubs.water.usgs.gov/circ1203/>
- 720 ODNR (2018). Ohio Coastal Atlas, Third Edition. <https://www.coastal.ohiodnr.gov/atlas>
- 721 Osborne, T. Z & Ron D. DeLaune. 2013. Soil and Sediment Sampling of Inundated
722 Environments. Chapter 2, page 21-40. *In*: R. D. DeLaune, K. R. Reddy, C. J. Richardson,
723 and P. J. Megonigal, eds. *Methods in Biogeochemistry of Wetlands*, Soil Science Society of
724 America. Madison, WI. 1024 pp.
- 725 Paton, D., & PENSERV Corp, Pa. (2012). An evaluation of the USDA ESAP program for
726 converting EM data to electrical conductivity at Goodale Research Farm using a GEM2 and
727 an EM38. Retrieved from <https://harvest.usask.ca/handle/10388/9097>
- 728 Rabot, E., Wiesmeier, M., Schlüter, S., & Vogel, H. J. (2018). Soil structure as an indicator of
729 soil functions: A review. *Geoderma*, 314, 122–137.
730 <https://doi.org/10.1016/J.GEODERMA.2017.11.009>
- 731 Romero-Ruiz, A., Linde, N., Keller, T., & Or, D. (2018). A Review of Geophysical Methods for
732 Soil Structure Characterization. *Reviews of Geophysics*, 56(4), 672–697.
733 <https://doi.org/10.1029/2018RG000611>
- 734 Romero-Ruiz, A., Linde, N., Keller, T., & Or, D. (2019). The Geophysical Signatures of Soil
735 Structure. *Eos*, 100. <https://doi.org/10.1029/2019EO112545>
- 736 Shanahan, P. W., Binley, A., Whalley, W. R., & Watts, C. W. (2015). The Use of
737 Electromagnetic Induction to Monitor Changes in Soil Moisture Profiles beneath Different
738 Wheat Genotypes. *Soil Science Society of America Journal*, 79(2), 459–466.
739 <https://doi.org/10.2136/SSSAJ2014.09.0360>
- 740 SSURGO (2012). Gridded Soil Survey Geographic Database (SSURGO) for Ohio. Available
741 online at the Available online at <http://datagateway.nrcs.usda.gov/> October 15, 2012.

- 742 Sposito, G. (2023). *soil*. *Encyclopedia Britannica*. <https://www.britannica.com/science/soil>
- 743 Stewart, B. A. (Ed.). (1990). *Advances in Soil Science*, 14. [https://doi.org/10.1007/978-1-4612-](https://doi.org/10.1007/978-1-4612-3356-5)
744 3356-5
- 745 Subburayalu SK, Slater BK (2013). Soil series mapping by knowledge discovery from Ohio
746 county soil map. *SSSAJ* 77:1254-1268. Available online at
747 <http://datagateway.nrcs.usda.gov/> October 15, 2012.
- 748 Totsche, K. U., Rennert, T., Gerzabek, M. H., Kögel-Knabner, I., Smalla, K., Spiteller, M., &
749 Vogel, H. J. (2010). Biogeochemical interfaces in soil: The interdisciplinary challenge for
750 soil science. *Journal of Plant Nutrition and Soil Science*, 173(1), 88–99.
751 <https://doi.org/10.1002/JPLN.200900105>
- 752 USDA (2019). Soil Survey Staff, Natural Resources Conservation Service, United States
753 Department of Agriculture. Web Soil Survey. Available online at the following link:
754 <http://websoilsurvey.sc.egov.usda.gov/>.
- 755 Vogel, H. J., Balseiro-Romero, M., Kravchenko, A., Otten, W., Pot, V., Schlüter, S., ... Baveye,
756 P. C. (2022). A holistic perspective on soil architecture is needed as a key to soil functions.
757 *European Journal of Soil Science*, 73(1), e13152. <https://doi.org/10.1111/EJSS.13152>
- 758 Ward, N. D., Patrick Megonigal, J., Bond-Lamberty, B., Bailey, V. L., Butman, D., Canuel, E.
759 A., ... Windham-Myers, L. (2020). Representing the function and sensitivity of coastal
760 interfaces in Earth system models. *Nature Communications*,
761 11(2458). <https://doi.org/10.1038/s41467-020-16236-2>
- 762 Young, I. M., Crawford, J. W., & Rappoldt, C. (2001). New methods and models for
763 characterising structural heterogeneity of soil. *Soil and Tillage Research*, 61(1–2), 33–45.
764 [https://doi.org/10.1016/S0167-1987\(01\)00188-X](https://doi.org/10.1016/S0167-1987(01)00188-X)
- 765
- 766
- 767
- 768
- 769
- 770
- 771
- 772

